Communications of the Geological Survey of Namibia, ***29*** *(2026), 1-42*

Revisiting the Alnöitic Tuffisite Diatremes in the Kainab Alkaline Province, Southern Namibia

Lorenz Kemmler[1,2*], R. Johannes Giebel[2,3], Benjamin F. Walter[1], Michael A. W. Marks[1], Paul H. Macey[4], Gregor Markl[1]

[1]Eberhard Karls University Tübingen, Department of Petrology and Mineral Resources, Schnarrenbergstraße 94-96, 72074 Tübingen, Germany
[2]Technische Universität Berlin, Department of Applied Geochemistry, Ernst-Reuter-Platz 1, 10587 Berlin, Germany
[3]University of the Free State, Department of Geology, 250 Nelson-Mandela-Drive, Bloemfontein 9300, South Africa
[4]University of Cape Town, Department of Geological Sciences, 13 University Avenue South, Rondebosch 7701, South Africa

*Corresponding author: <lorenz.kemmler@gmail.com>

Abstract :- This study examines carbonate-bearing diatremes, dykes, and sills of the Kainab Alkaline Province in the Garub valley, southern Namibia. The valley hosts some 100 genetically related magmatic bodies covering ~3000 km² and marking the north-eastern extent of the Kuboos-Bremen Line, a NE-SW-trending line of Pan-African intrusive complexes extending over 270 km from South Africa into Namibia. To study the petrogenesis of the rocks, a combination of petrography, whole-rock geochemistry, micro-X-ray fluorescence, scanning electron microscopy and stable isotope analysis, were employed.

The studied samples feature macrocrystic phlogopite and diopside, along with bleached xenoliths of gneiss and sandstone, set in a fine-grained groundmass of dolomite, albite, and quartz, with minor modal amounts of magnetite, rutile, and apatite. Some samples contain phlogopite, diopside, clinochlore, calcite, and baryte, an unusual assemblage in ultramafic and carbonatitic rocks. The diatremes and dykes are surrounded by metasomatic halos, characterised by bleached wall-rock gneiss, enriched in Na (albitisation). Concurrently, the intrusives themselves were contaminated by the wall rock, thereby assimilating Si, Al and K. Mineral assemblages formed under explosive, hypabyssal conditions (fluidisation), as indicated by rock textures. These assemblages comprise a mixture of xenocrystic material, magmatic phases, and hydrothermal products, which is supported by textural evidence and stable isotope data.

This unique suite of rocks is classified as hypabyssal dolomite silico-carbonatite with a distinct ultramafic lamprophyre affinity. Trace element ratios, together with literature data, suggest a carbonated garnet peridotite melt source, partially molten due to asthenospheric upwelling. Two distinct melt types were identified: an ultramafic melt (Type 1: diopside, phlogopite, dolomite) and a carbonatitic melt (Type 2: dolomite, albite, apatite, magnetite), both of which have been preserved in pelletal lapilli within halos of relatively uncontaminated melt. Derived from the same source, these melts probably resulted from liquid immiscibility. The emplacement of these diatremes occurred in the early Cambrian, probably along pre-existing Tonian NNE-trending brittle structures which were reactivated during the regional-scale crustal warping in advance of the evolving Damara and Gariep orogens.
.

Keywords :- Carbonatite, Great Karas Mountains, Volcanism, Pan-African, Fluids

Introduction

Carbonatites, kimberlites, and ultramafic lamprophyres (UMLs) are commonly associated with each other (e. g. Smith *et al.*, 2013; Mattsson *et al.*, 2019; Tappe *et al.*, 2017; Dongre and Tappe, 2019) and originate from mantle sources, although their exact compositions and depths are still under debate (e. g. Rock, 1986; Tappe *et al.*, 2006; Yaxley *et* *al*., 2021). This implies a shared origin of these rocks from deep-seated, volatile-rich magmas (Tappe *et al*., 2006; Foley *et al*., 2019), likely derived from low-degree partial melting of carbonated peridotite in a depleted mantle, possibly influenced by phlogopite-rich metasomes (Downes *et al*., 2005; Prokopyev *et al*., 2020). Both, garnet and spinel peridotite are considered viable sources (Dasgupta *et al*., 2009; Yaxley *et al*., 1991), and are commonly found in UMLs (Tappe *et al*., 2005). These melts may rise rapidly through the lithosphere - within 10 hours to 2 days (Sparks *et al*., 2006) - via volatile exsolution and fractional crystallisation (Giuliani *et al*., 2020). As SiO_2 increases, CO_2 solubility decreases, triggering fluid exsolution and accelerating magma ascent (Russel *et al*., 2012, 2019), which results in typically explosive emplacement. Thus, kimberlites and, less commonly, UMLs and carbonatites form hypabyssal intrusions (dykes, sills) and volcanoclastic pipes (diatremes) containing abundant country rock xenoliths, mantle-derived xenoliths and magmaclasts (Smith *et al*., 2018). The partial melting, giving rise to these rather exotic rocks, may be triggered by asthenospheric upwelling or mantle plumes (Bell and Tilton, 2001; Davies and Rawlinson, 2014). The relationship between kimberlites and carbonatites remains under dispute. Some models propose that ascending carbonatite melts assimilate mantle material, thus becoming enriched in SiO_2 and evolving into hybrid magmas resembling kimberlites (Kjarsgaard *et al*., 2009; Kamenetsky, 2016).

The ~100 diatremes and associated intrusions (dykes and sills) of the Kainab Alkaline Province (KAP) in southern Namibia were initially described by Verwoerd (1967), and subjected to more detailed investigations by Schreuder (1975). These two studies remain the only comprehensive assessments of the site to date. However, the rocks remain poorly understood, including their proper classification. Various authors have proposed affinities with carbonatites, kimberlites, lamprophyres or olivine melilitites, underscoring the petrological and genetic complexity of these bodies (Schreuder, 1975; Spriggs, 1988; Verwoerd, 1993; Miller, 2012). The intrusive mode is referred to as tuffisite diatremes (Schreuder, 1975), but peperites have been proposed as well (Verwoerd, 1967). Recent advances in the understanding of carbonatite-related systems, alongside improved analytical techniques and geodynamic models, provide a timely opportunity to reassess this enigmatic occurrence. This contribution aims to identify the processes involved during volcanism in the KAP, the nature of the parental magma and, finally, to propose a revised classification of this occurrence. In addition, the genetic link of these diatremes with the contemporaneous intrusive complexes of the Kuboos-Bremen Line (Reid, 1991) is evaluated, as recent dating shows that not all initially proposed intrusives are related in age (Zech *et al*., 2025). To further put the KAP field into context, its carbonatitic characteristics are examined and compared with neighbouring and analogous carbonatite occurrences such as Mickberg, Weltevrede, Gross Brukkaros, and Marinkas Quelle.

The Garub intrusives share key characteristics with ultramafic lamprophyres, which typically contain macrocrysts of phlogopite and olivine. These rocks are further classified into three types: alnöite (melilite-bearing), aillikite (carbonate-rich), and damtjernite (containing nepheline and/or alkali feldspar; Rock, 1986; Tappe *et al*., 2005).

Carbonatites are igneous rocks with ≥25–50 vol.% primary carbonate minerals (Le Maitre *et al*., 2002; Mitchell, 2005; Tappe *et al*., 2025), which are classified by the dominant carbonate into calcite-, dolomite-, ankerite-/siderite- (“ferro-”) and nyerereite-/gregorite- (“natro-“) carbonatites (Yaxley *et al*., 2022). They occur in extrusive, intrusive, and carbothermal forms, commonly associated with ultramafic or alkaline rocks (Woolley and Kjarsgaard, 2008; Schmidt *et al*., 2024). Carbonatite genesis remains debated, with hypotheses including mantle-derived primary carbonate melts, residual melts from fractional crystallisation of carbonate-bearing silicate melts, and products of silicate-carbonate immiscibility (Yaxley *et al*., 2021; Schmidt *et al*., 2024). Many intrusive types represent cumulates or evolved melts (Veksler *et al*., 1998; Kamenetsky *et al*., 2021), modified by fluid interaction, creating high-salinity brines (Prokopyev *et al*., 2016; Anenburg *et al*., 2021; Walter *et al*., 2021). Carbonatite magmas and associated fluids alter host rocks, forming fenites characterised by albite, orthoclase, aegirine, and amphibole (Le Bas, 2008; Elliot *et al*., 2018). Interaction with crustal material may also produce Fe-Mg silicates such as olivine, clinopyroxene, and mica (Giebel *et al*., 2019; Vasyukova and Williams-Jones, 2022).

Kimberlites are deep-origin volcanic rocks (150–250 km) known for transporting diamonds and mantle materials rapidly to the surface (Haggerty, 1994; Sparks, 2013). They typically contain olivine macrocrysts (20–30 vol.%) set in a matrix of olivine, spinel, phlogopite, perovskite, apatite, monticellite, and calcite, along with late-stage carbonates and serpentinite. Accessory macrocrysts may include pyrope, ilmenite, Cr-diopside, and diamonds (Mitchell *et al.*, 2019; Sparks *et al.*, 2006).

Geological Setting

Regional Geology

The Kainab Alkaline Province (KAP; formerly referred to as the Garub intrusions or the Grünau Alkaline Province; Schreuder, 1975; Winter and Rikhotso, 1998) bodies are hosted within rocks of the Namaqua–Natal Metamorphic Province (NNMP), a polyphase Mesoproterozoic (~1.35-1.0 Ga) orogenic belt that extends from eastern South Africa to the central Namibian coastline (e. g. Bial *et al.*, 2016; Macey *et al.*, 2022; Fig.1). In southern Namibia, the NNMP is subdivided into three NW-trending tectonic domains. The Palaeoproterozoic (1.91-1.86 Ga) arc-related (meta-)volcanic and (meta-)plutonic rocks of the Richtersveld Subprovince are tectonically overlain by Mesoproterozoic metapelitic granulites and granitic orthogneisses (~1.22-1.16 Ga), and late- to post-tectonic granitoids (~1.12-1.08 Ga) of the Kakamas Domain (Fig.1). The Richtersveld Subprovince and Kakamas Domain are separated by the Lower Fish River-Onseepkans Thrust Zone, a ~50km-wide, low-angle tectonic damage zone consisting of slices of both the Richtersveld Subprovince and the Kakamas Domain, interlayered with exotic sheets of 1.81 Ga and ~1.31-1.26 Ga orthogneisses. The main NW-trending regional penetrative gneissic foliation resulting from isoclinal folding and thrusting during the main Namaqua Orogeny (~1.20-1.12 Ga) was refolded into large, kilometre-scale dome- and basin folds, and subsequently reworked along major, discrete, subvertical NW-trending transcurrent shear zones (~1.0-0.96 Ga) intruded by coeval leucogranite and pegmatite (Macey *et al.*, 2022 and references within).

Extension of the Namaqua (Kalahari Craton) crust in the mid-Tonian led to the emplacement of granitic to syenitic plutons, plugs and ring complexes (and volcanic equivalents) of the Richtersveld Igneous Suite (903–771 Ma, Frimmel *et al.*, 2001; Zech *et al.*, 2025), and the intrusion of the ~150 km-wide NNW to NNE-striking Gannakouriep mafic dyke swarm (~790 Ma, Rioux *et al.*, 2010) that extends for more than 300 km from Kleinzee in South Africa to north of Grünau in Namibia. Continued extension resulted in the development of a basin into which the Gariep Supergroup (mostly arenite, mudstone and diamictite) was deposited (e. g. Frimmel, 2008). Tectonic inversion and the closure of the Gariep Basin during the assembly of Gondwana began approximately 555 Ma ago, resulting in the formation of the southeast-vergent, greenschist-facies Gariep fold-and-thrust belt, which was thrust over the NNMP. The crustal flexure in the foreland of the developing Gariep Orogen formed basins into which the late Ediacaran to Cambrian Nama Group sediments were deposited onto NNMP basement rocks (~555–500 Ma; e. g. Allsopp *et al.*, 1979; Saylor *et al.*, 2005; Nelson *et al.*, 2022).

The Kuboos-Bremen Suite, a NE-trending line of Cambrian granitic, syenitic and carbonatite plutons, ring complexes, plugs, breccias, and dykes intruded the NNMP basement and Nama Group at the end of the Gariep Orogeny (Fig. 1A; e. g. Reid, 1991; Zech *et al.*, 2025). Following a period of stability, the NE-striking Karasburg graben developed in southern Namibia as a fault-bounded peripheral basin to the developing main Karoo basin, into which the Carboniferous Dwyka Group (comprising shales and diamictite) and Permian Ecca Group (mudstone, siltstone, sandstone) were deposited unconformably on top of the NNMP and Nama Group. Post-Karoo dolerites intruded during the Jurassic break-up of Eastern Gondwana (~185 Ma; Siedner and Mitchell, 1976).

Several phases of brittle tectonics have occurred since the end of the Namaqua Orogeny, with post-Gannakouriep faults and fractures controlled by pre-existing Namaquan (NW-trending) and Gariepian (N- to NE-trending) structures (e. g. Muir *et al*, 2023).

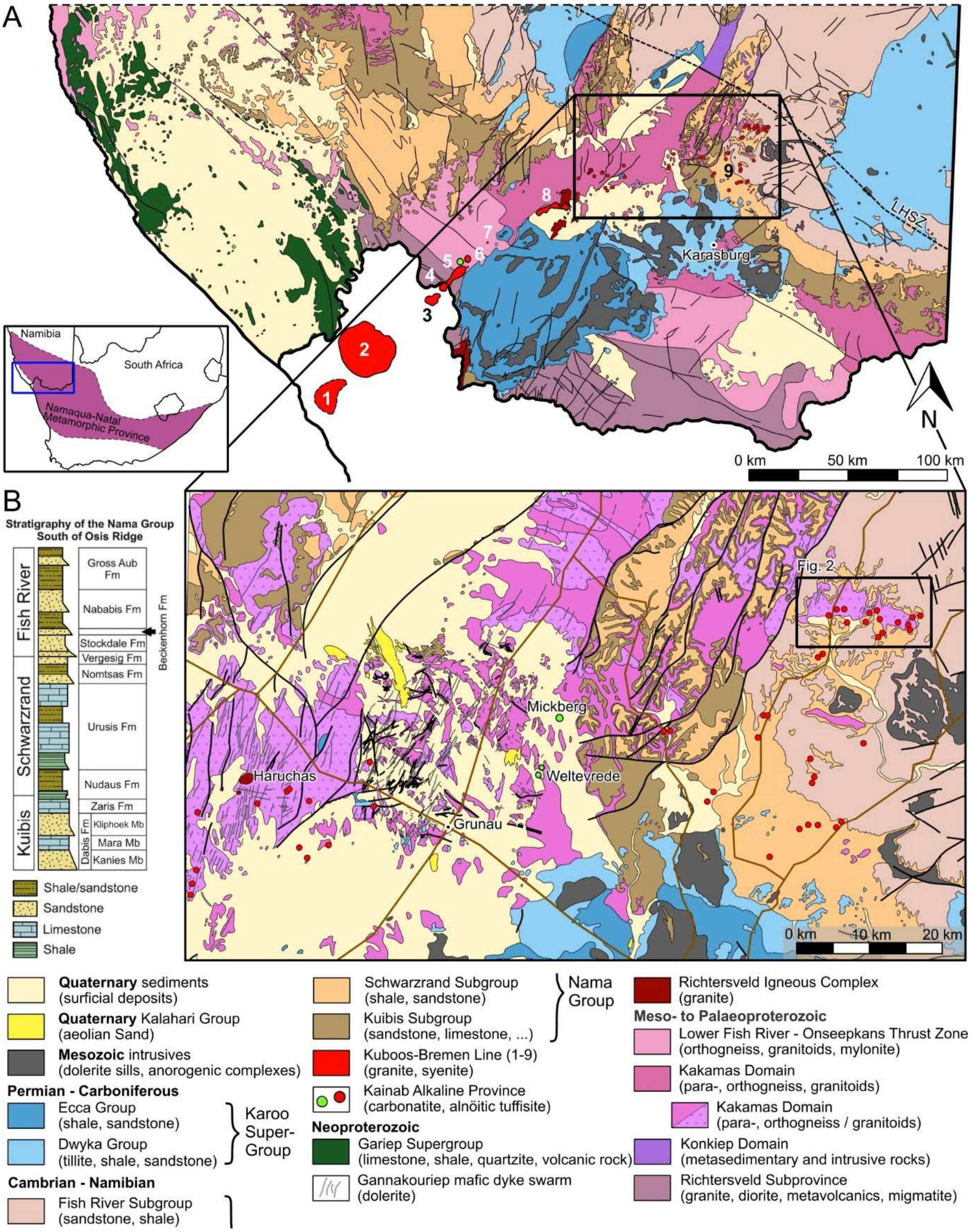

Figure 1. A) Regional geological map of southern Namibia, featuring intrusive complexes of the Kuboos-Bremen Line (1-9; Appendix 1) - bottom left: extent of the NNMP; GIS data obtained from Geological Survey of Namibia, KBL locations after Reid (1991); B) Geological map of the Kainab Alkaline Province showing intrusive locations (red dots), confirmed carbonatite occurrences (after Schreuder 1975, green dots); left: stratigraphy of the Nama Group in southern Namibia (adapted from Walter *et al*., 2023; originally from Germs,1983)

Kuboos-Bremen Line (KBL) and Kainab Alkaline Province (KAP)

The KBL was first described by Söhnge and De Villiers (1948) and is composed of nine intrusive complexes extending over 270 km from the Atlantic Coast in South Africa to the Grünau area (Reid, 1991; Fig. 1A). From SW to NE these include the Swartbank, Kuboos and Tatasberg complexes in South Africa, as well as the Namibian Grootpenseiland, Marinkas Quelle, Kanabeam intrusive complexes, the Mt. Ai-Ais breccia pipe, the Bremen igneous centres and the Kainab Alkaline Province (KAP; Appendix 1). While granites and quartz-syenites dominate in the southwest (Swartbank, Kuboos, and Tatasberg), syenites and foid-syenites become increasingly prominent towards the northeast (Grootpenseiland, Marinkas Quelle and Kanabeam). Marinkas Quelle and the much smaller Mickberg and Weltevrede bodies of the KAP are currently the only recognised carbonatite occurrences of the KBL (Verwoerd, 1993). The KBL cuts across several Precambrian tectonic boundaries, intruding the Namaqua domains, the Gariep Belt, and the overlying Nama Group. Radiometric age data for the different complexes of the KBL range from ~536 to 492 Ma, indicating intrusion during the Pan-African orogeny (Allsopp *et al*., 1979; Smithies, 1991; Zech *et al*., 2025).

Being part of the KBL, the KAP comprises about 100 diatremes, dykes and sills of carbonate-rich mafic alkaline rocks within an ENE-trending zone extending from farm Garub 266 to the Dreikopf Hills west of the Bremen Complex (Fig. 1B). They were discovered during regional mapping from 1938 to 1939 by J. T. Wessels (unpublished) and first described by Verwoerd (1967), later by Schreuder (1975) and briefly mentioned in an unpublished prospecting report (Winter and Rikhotso, 1998), which represent the only studies of the KAP to date. Subsequent publications largely rely on Schreuder’s findings with only limited new additions (e. g. Verwoerd, 1993; Miller, 2012). In the central part of the KAP (10 and 20 km northeast of Grünau) two carbonatite occurrences are recognised: 1) Weltevrede , composed of two breccia plugs of variable carbonate contents, with cross-cutting ankeritic carbonatite dykes (Walter *et al*., 2025), and 2) Mickberg, a 100 m tall double-crested hill, composed of Namaqua gneiss, intruded and brecciated by ankeritic carbonatite (Schreuder, 1975).

The largest concentration of carbonate-bearing eruptives of the Kainab Alkaline Province is situated on farm Garub 266, within an erosional window/valley traversed by the predominantly dry Kainab River drainage. This valley, which is located 80 km north of Karasburg at an elevation of approximately 1200 m within the Great Karas Mountains, hosts around 60 mapped KAP occurrences. These are distributed along the farm road that traverses the valley in an E-W direction (Fig. 2; Verwoerd, 1967). The valley floor consists of medium-grained gneisses of the Kakamas Domain (Schreuder, 1975; Macey *et al*., 2022), likely belonging to the Narries Group (granulitic metapelite) and/or Eendoorn Suite (garnet-bearing augen gneiss) that have been dated between 1220 and 1190 Ma (Nordin, 2009; Macey *et al*., 2022). Within the Garub valley, there are no significant mapped structures except for the NW-SE striking gneissic foliation and roughly SSW-NNE striking Gannakouriep doleritic dykes (Fig. 2). About 6 km to the north, the Lord Hill-Excelsior Shear Zone (LH-ESZ) separates the Kakamas Domain from the Konkiep Domain (Macey *et al*., 2022). West of the valley lies a series of five NNE-SSW striking faults that have been interpreted as reverse faults (Schreuder, 1975). An angular unconformity separates the Kakamas Domain from the overlying late Neoproterozoic to early Cambrian Nama Group, which is subdivided into the Kuibis, Schwarzrand, and Fish River Subgroups (Germs, 1983). Although the Kuibis Subgroup is well developed elsewhere within the KAP, it is absent in the Garub valley. The Schwarzrand Subgroup comprises a succession of greyish-green quartzite, sandstone, sandy shale, siltstone, and brown and yellow weathering dolomitic limestone (Fig. 3D; Schreuder, 1975; Spiering *et al*., 2023). The Schwarzrand Subgroup in the Garub valley is significantly thinner (80 m) than in other regions (Schreuder, 1975). Eight volcanic ash beds from the Schwarzrand Subgroup (~125 km SW of the Garub valley) have been dated by U-Pb zircon methods and yield ages from about 545 Ma at the base to about 539 Ma at the top (Nelson *et al*., 2022; Linnemann *et al*., 2019). The Fish River Subgroup conformably overlies the Schwarzrand Subgroup and forms the capping strata of the

Great Karas Mountains, east of the aforementioned reverse faults. It is typically red to purple in colour and composed of sandstones and shales (Geyer, 2005). The whole sedimentary cover reaches a thickness of around 130 m.

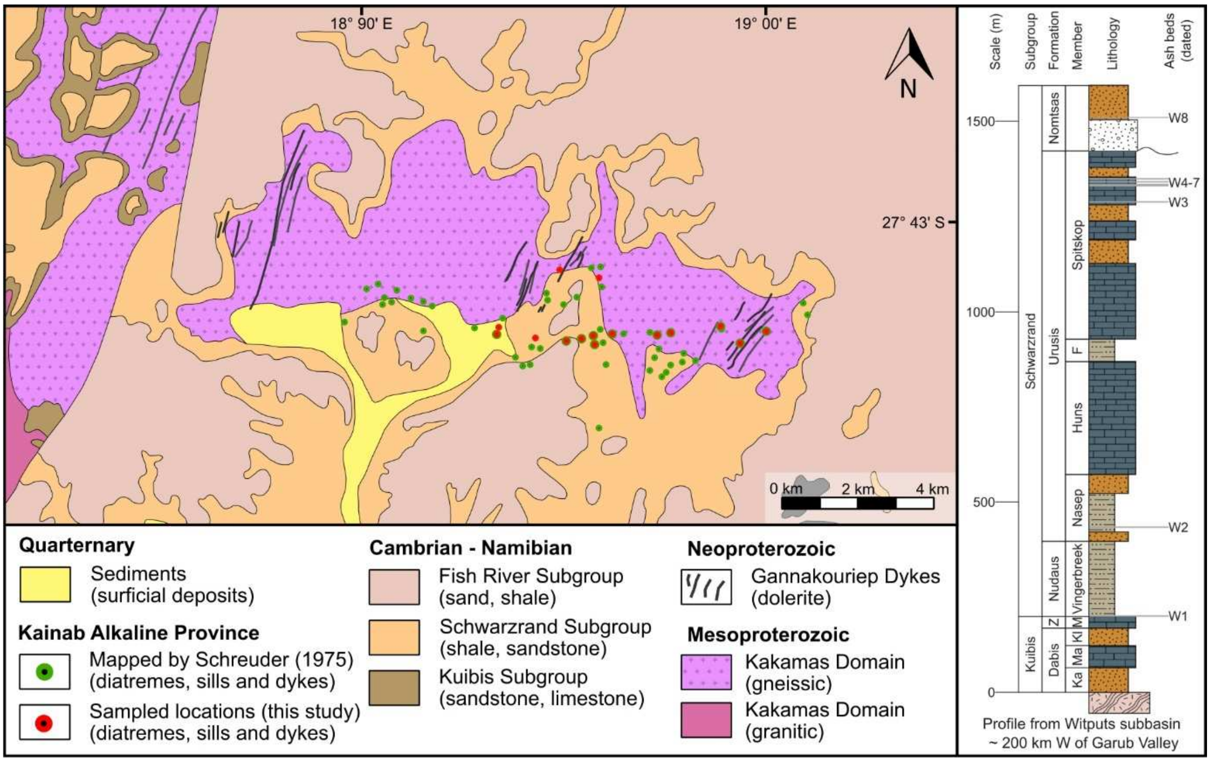

Figure 2. Geological map of the Garub valley with intrusive locations mapped by Schreuder (1975; green) and locations of occurrences sampled during this study (red); on the right is a stratigraphic profile of the Schwarzrand Subgroup from the Witsputs Subbasin around 200 km west of the Garub valley including dated ash beds W1-W8 (Spiering *et al*., 2023). Please note that this profile has a thickness of around 1500 m while the Schwarzrand Subgroup is only around 80 m thick within the Garub valley, where it nevertheless has a correlating stratigraphy.

Igneous rocks of the KAP include diatremes, dykes, and sills (Schreuder, 1975), with the latter two often emanating from the former (Fig. 3E). The diatremes have diameters of up to 50 m (Figs 3A-B) and may be composed of multiple generations of diatreme facies, indicated by different colours, textures, and xenolith types and abundance (Fig. 3H). Xenoliths are commonly fist-sized but range from <1 mm to tens of centimetres (Fig. 3F). They are either of sedimentary (Schwarzrand Subgroup) or metamorphic (Namaqua basement gneisses) origin, with the latter type often being bleached (Figs 3F-G). The dykes typically appear as brown or dark-brown ridges, are up to about 5 m wide, can be traced for up 500 m, and are usually directly associated with the diatreme bodies (Fig. 3E). Some dykes are controlled by joints or foliation in the wall rock, while others are randomly oriented and sinuous. The sills are typically emplaced above or below limestone layers of the Schwarzrand Subgroup (Fig. 3D). They vary in thickness, ranging from a few centimetres to two metres, commonly exhibiting a lenticular shape. The oldest determined age from a pyroclastic sill in the eastern Garub valley is 491 ± 8 Ma (Rb-Sr analyses on whole rock and biotites; Allsopp *et al*., 1979). Biotite Ar-Ar dating on lamprophyric carbonate dykes yield ages of 523 and 527±2 Ma (Zech *et al*., 2025), confirming previous Ar-Ar (514–524 Ma) ages on biotite from dykes outcropping ~30 km south of the Garub valley (Spriggs, 1988).

At its eastern extent, the Garub valley hosts an abandoned lead-fluorite mine, which is believed to have operated between 1922 and 1939 (Schreuder, 1975, and references therein). The deposit is situated at the contact between Namaqua basement gneiss and a tuffisite diatreme, with a nearby associated dolerite dyke. In addition to fluorite, minor amounts of Pb-, Fe-, Cu- and Ag-sulfides, along with their supergene reaction products, as well as baryte, calcite, and quartz, have been reported. Walter *et al*. (2024) suggest that the fluorite deposit is unlikely to have formed as a direct result of diatreme magmatism. Instead, the diatreme probably served as a fluid migration pathway or structurally weak zone that facilitated the deposit's formation during Mesozoic times (Walter *et al*., 2024).

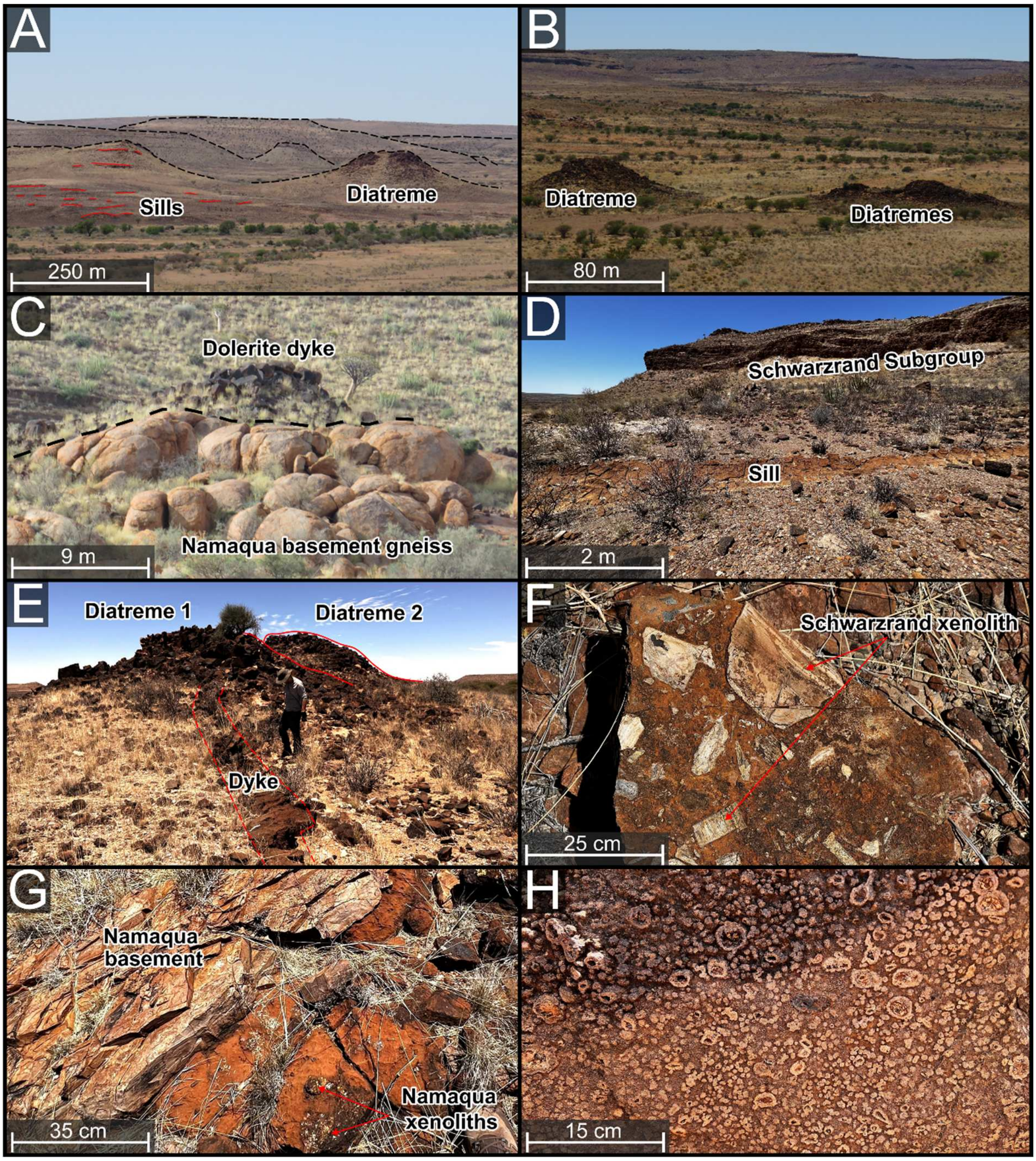

Figure 3. A) View of two large diatremes with small dykes to the left (marked in red) and the Nama escarpment in the background; B) Three medium-sized diatremes, two of which are adjacent, with escarpments in the background; C) Spherically weathered Namaqua gneiss/granite with dark doleritic dyke in the background; D) Schwarzrand escarpment featuring alternating limestone and sandstone, with a small sill in the foreground; E) Small diatreme with a cross-cutting dyke; F) Block of diatreme breccia containing xenoliths of various sizes and types; G) Outcropping of xenolith-rich diatreme breccia next to Namaqua basement; H) Spherical textures in a diatreme locally containing xenoliths (sample GRB039)

Sample Material and Analytical Methods

A total of 50 fist-sized rock samples were collected, representing 15 diatremes and associated dykes and sills and their country rocks (Appendix 2). Several of the diatreme samples are rich in xenoliths of Namaqua gneisses (Figs 4B, D-F & H) or, in some cases, of sedimentary rocks of the Schwarzrand Subgroup (Figs 4B-C).

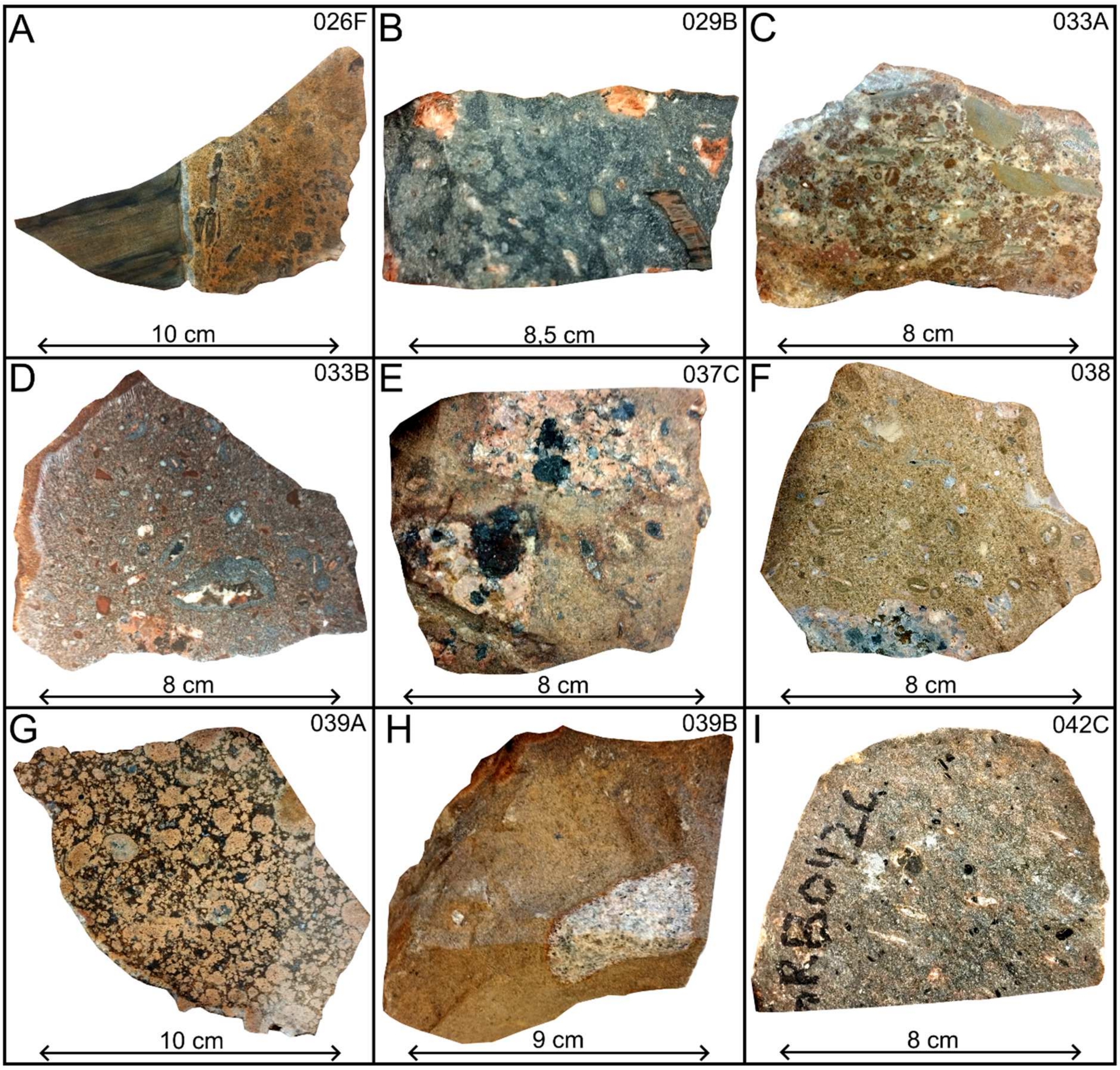

Figure 4. Montage of selected samples showcasing their diversity: A) Contact between Schwarzrand limestone and diatreme; B) Grey matrix diatreme with Schwarzrand Subgroup and Namaqua gneiss xenoliths, exhibiting slight globular textures; C) Strongly brecciated diatreme with multiple xenolith types of various sizes; D) Similar brecciation but with a differently coloured matrix and circular grey zones around the xenoliths; E) Large, bleached xenoliths of gneiss within diatreme facies; F) Altered large xenolith in a matrix hosting smaller clasts surrounded by darker, rounded rims; G) Dark-brown matrix with lighter-brown globules, some of which contain clasts; H) Large bleached gneissic xenolith within a xenolith-free matrix; I) Greyish matrix containing black phlogopite and small clasts

For petrographic study, thin sections of 40 samples were investigated by transmitted and reflected light microscopy, and by micro-x-ray fluorescence analysis (M4 Tornado by Bruker) at the mineralogical and geochemical micro-analytical laboratory (MAGMA-Lab) of the Department of Applied Geochemistry (Technische Universität Berlin, Germany). The latter was equipped with a Rh tube, run with 50 kV using a beam current of 600 µA with a beam diameter of 20 µm. The measuring point distance was 20 µm, with a measuring time of 30 ms per analysis spot using the area mode. Scanning electron microscopy (SEM) analysis was conducted at the Department of Geosciences, Universität Tübingen (Germany) with two tabletop instruments (Phenom XL and TM3030+) run with an acceleration voltage of 15 kV at the BSE mode using a focused beam.

Whole-rock major and minor element geochemistry was determined on 35 samples by wavelength dispersive XRF (S8 Tiger, Bruker) on fused beads (Li-tetraborate/-metaborate: sample ratio = 2:1) at the MAGMA-Lab. Element concentrations were quantified using the GeoQuant calibration package (Bruker). The loss on ignition (LOI) was determined as the percentage weight difference between the dried (105°C for 24 hours) and annealed sample powder (1200°C for 3 hours). LOI was accounted for in the XRF quantification; the mean total XRF sums (oxides plus LOI) ranged between 99 to 101 wt.% for most samples, with a few exceptions at 95 and 105 wt.%. Since the LOI values were not used as weathering indicators, no further corrections were applied. Calibration was conducted using 32 standards, with defined lower and upper limits for element concentrations.

Total sulfur and total carbon analyses were carried out with the Carbon-Sulfur-Analyser CS-2000 (ELTRA) at the Laboratory for Environmental and Raw Materials Analysis (LERA, Karlsruhe Institute for Technology, Germany). The accuracy (<0.2 %) and reproducibility (<6 %) was checked by correlation with certified reference materials (steel, bariumsulfate). Trace element and REE were determined by ICP-MS (iCAP, Thermo Fisher Scientific; LERA) after HNO_3-HF-$HClO_4$-HCl acid digestion of powdered sample material (100 mg). For complete silicate decomposition, the pre-oxidised sample was digested with HF and $HClO_4$ in a sealed Teflon vessel at 120 °C for 16 hours. After evaporation, it was re-dissolved in HNO_3 and HCl, purified by triple evaporation, and finally dissolved in 50 ml of ultrapure water. The precision of the ICP-MS measurement was in the range of 1 %. Measurement quality was checked regularly, with 5 µg/l standard element solutions. The precision and the accuracy of the whole process, including acid digestion, was monitored by inserting certified reference materials CRM-Sy2 and GRE03 (High-Purity standards, Inc.) into the measurement sequence at ten sample intervals (SD is between 1 % and 8 % for most elements).

Stable isotope ($\delta^{13}C$, $\delta^{18}O$) analyses were also conducted on seven samples from the Garub valley and six samples from the wider Kainab Alkaline Province (LERA). Carbonate-rich samples (0–80% calcite, 20–100% dolomite/ankerite) were analysed for stable isotope ratios ($\delta^{13}C$, $\delta^{18}O$) using a GasBench II gas chromatography system (Thermo Fisher Scientific). Sample sizes were adjusted to ensure a carbonate signal >40 µg C, and samples were ground to µm-sized fractions for full reaction with phosphoric acid. Following Al-Aasm *et al*. (1990) and Baudrand *et al*. (2012), carbonates were analysed without prior separation, leveraging their different reaction rates: calcite reacted at 25 °C for 2 hours, while residual carbonates reacted at 50 °C for 24 hours after an intermediate flushing step. Samples were reacted in Gas Bench II vials at 25 and 50 °C, flushed with He, and injected with acid. The evolved CO_2 was analysed by Delta V Advantage IRMS, with each sample measured ten times. Accuracy was assessed using in-house Carrara marble and certified standards (NBS-18, IAEA CO-1). Dolomite and ankerite data were corrected according to Kim *et al*. (2015). Replicate analysis confirmed a precision of ±0.05 ‰ for $\delta^{13}C$ and $\delta^{18}O$.

Petrography

Wall Rocks

Namaqua samples (GRB037B, GRB 040C, GRB041A) are porphyroblastic garnet gneisses (Kakamas Domain) comprising quartz, alkali feldspar, plagioclase, garnet (almandine), biotite, muscovite and sillimanite, with minor amounts of rutile, zircon, and monazite. Most feldspars are turbid, elongated alkali feldspars with perthitic textures, along with smaller, more circular grains of albite-oligoclase, often containing biotite inclusions. The rock also contains heavily serpentinised minerals, displaying an oil film-like colour with iron-rich phases remaining in the cracks. Muscovite is slightly bent and often associated with biotite and sillimanite (Fig. 5H). Garnets frequently contain inclusions of quartz and biotite. Gneissic xenoliths or direct contacts with the diatremes are heavily altered, featuring albite, quartz, and serpentinised and chloritised minerals. Since xenocrystals from the Namaqua wall rocks are often present in significant proportions in the diatremes, they are included in the paragenetic sequence to indicate alteration reactions (Fig. 6).

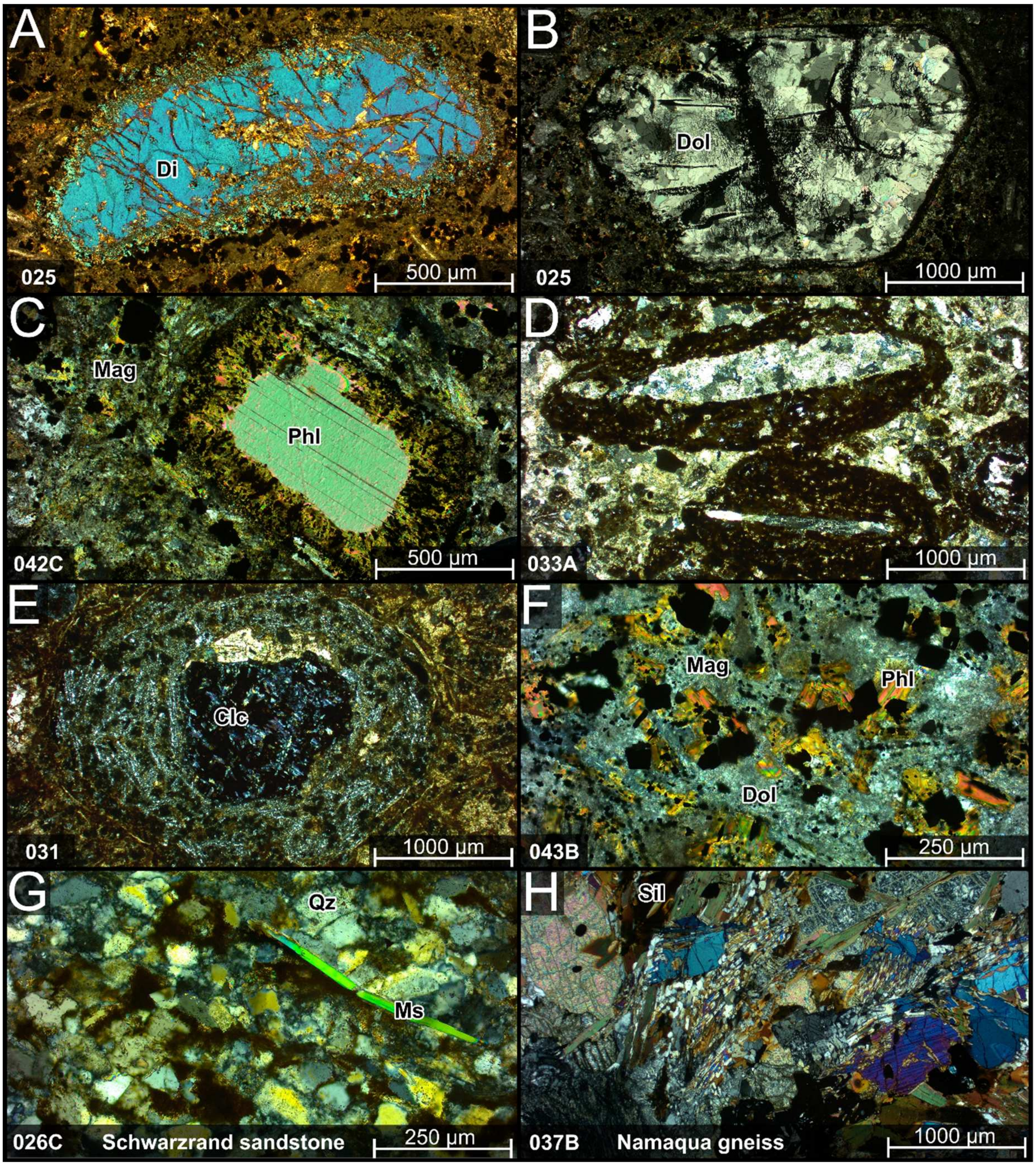

Figure 5. Photomicrographs of selected minerals, textures and lithologies: A) Altered diopside with blue interference colours; B) Spherical rims composed of multiple equigranular dolomites, likely of replacive origin; C) Phlogopite macrocrysts with zone of alteration; D) Two pelletal lapilli in matrix containing elongated xenolith surrounded by a dark halo; E) Heavily chloritised phenocryst with anomalous blue interference colours, featuring a spherical rim and prevalent black iron phases; F) Phlogopite-rich matrix along with magnetite, dolomite, and albite; G) Fine-grained sandstone from the Schwarzrand Subgroup, composed of quartz with minor muscovite; H) Gneissic Namaqua basement, consisting of quartz, plagioclase, perthitic K-feldspar, minor sillimanite, and biotite, along with rounded, serpentinised (?) grains with high interference colours

Samples of the Schwarzrand Subgroup include limestone (GRB026B, GRB029A) and quartzitic sandstone (GRB026C, GRB026F). The micritic dolomitic limestone features areas of light, transparent dolomite and brownish regions, reflecting small-scale stratigraphic variations. They contain carbonate veins and pockets of larger, optically clear calcite, with zones of oxidation, forming brown, colloform-like rims emanating from these veins. Other minerals are not present in observable quantities. The sandstones are fine-grained, predominantly composed of angular quartz with minor feldspar, some displaying pericline twinning (Fig. 5G). Infrequent muscovite and occasional zircon may be present. Macroscopic bedding structures may occur (Fig. 7D), while thin veins of quartz may cross-cut the strata. Occasional sandstone xenoliths within the diatreme are angular and do not show any reactive halos opposed to the Namaqua wall rock (Fig. 8C).

Diatreme Facies

Samples from diatremes, dykes, and sills are similar optically, petrographically and geochemically, but have varying amounts of xenoliths, phenocrysts, and globular textures, which are used to discriminate rock types.

Most samples feature a matrix of calcite or iron-bearing dolomite, with variable amounts of albite/oligoclase, magnetite, rutile, quartz, clinochlore and phlogopite (Figs 5F & 9E). Dolomite appears as enclosed remnants within magnetite or phlogopite and as larger matrix-forming grains. Small anhedral or acicular albite/oligoclase grains may form tangentially around clasts of various compositions (Fig. 5E). Phlogopite is partially replaced by albite, which is also interstitial to dolomite (Fig. 9E). Small books of clinochlore frequently exhibit anomalous blue interference colours near or within altered xenolith remains (Fig. 5E). Small, evenly dispersed, typically euhedral rutile is often accompanied by magnetite. Subordinate euhedral apatite and, in some samples, baryte are also present, with tiny euhedral apatite crystals within phlogopite. Minor ilmenite, euhedral pyrite, and uncommon chalcopyrite occur locally (Figs 9C-E). A paragenetic sequence is divided into a basement section (Namaqua) and a magmatic and hydrothermal stage (diatreme facies; Fig. 6).

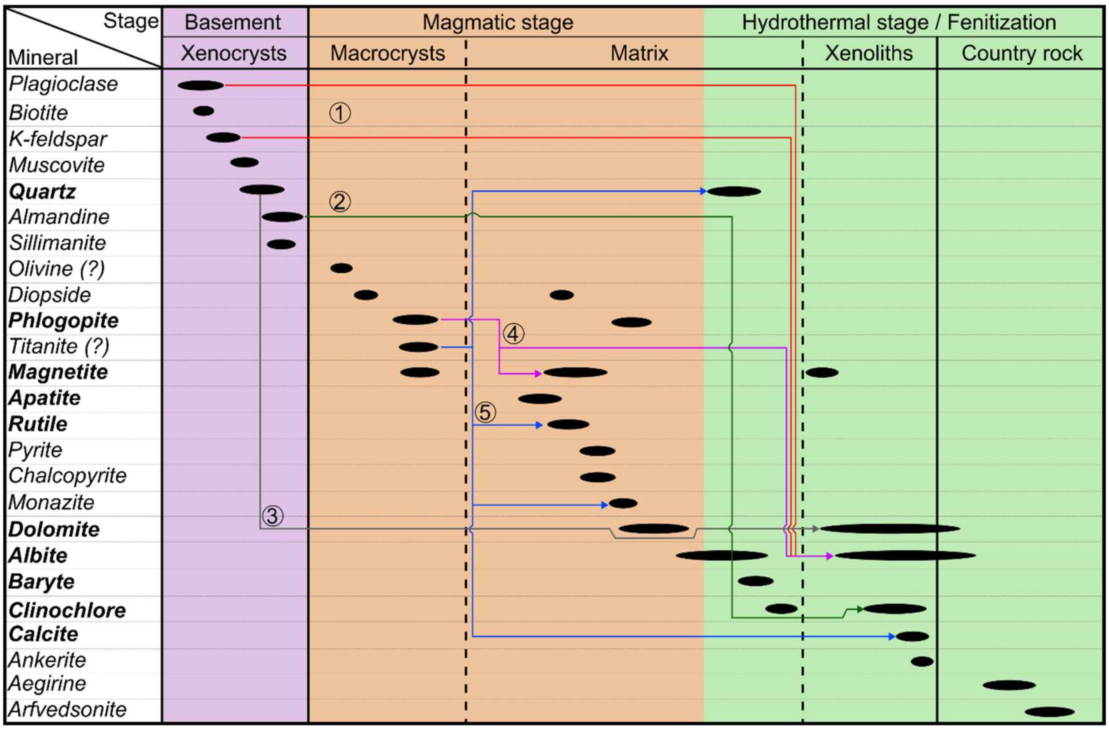

Figure 6. Paragenetic sequence of the Namaqua gneissic basement, the KAP intrusives (including macrocrysts and matrix), embedded Namaqua xenoliths, and the fenitised country rock (macroscopic contact samples): the sequence includes a magmatic stage and a hydrothermal stage, with a continuous transition between them. Minerals that constitute most of the intrusive samples are shown in bold type, while altered and now unidentifiable minerals are identified by a question mark (?). Alteration reactions and replacements are indicated by arrows with corresponding numbers, which are explained in the discussion.

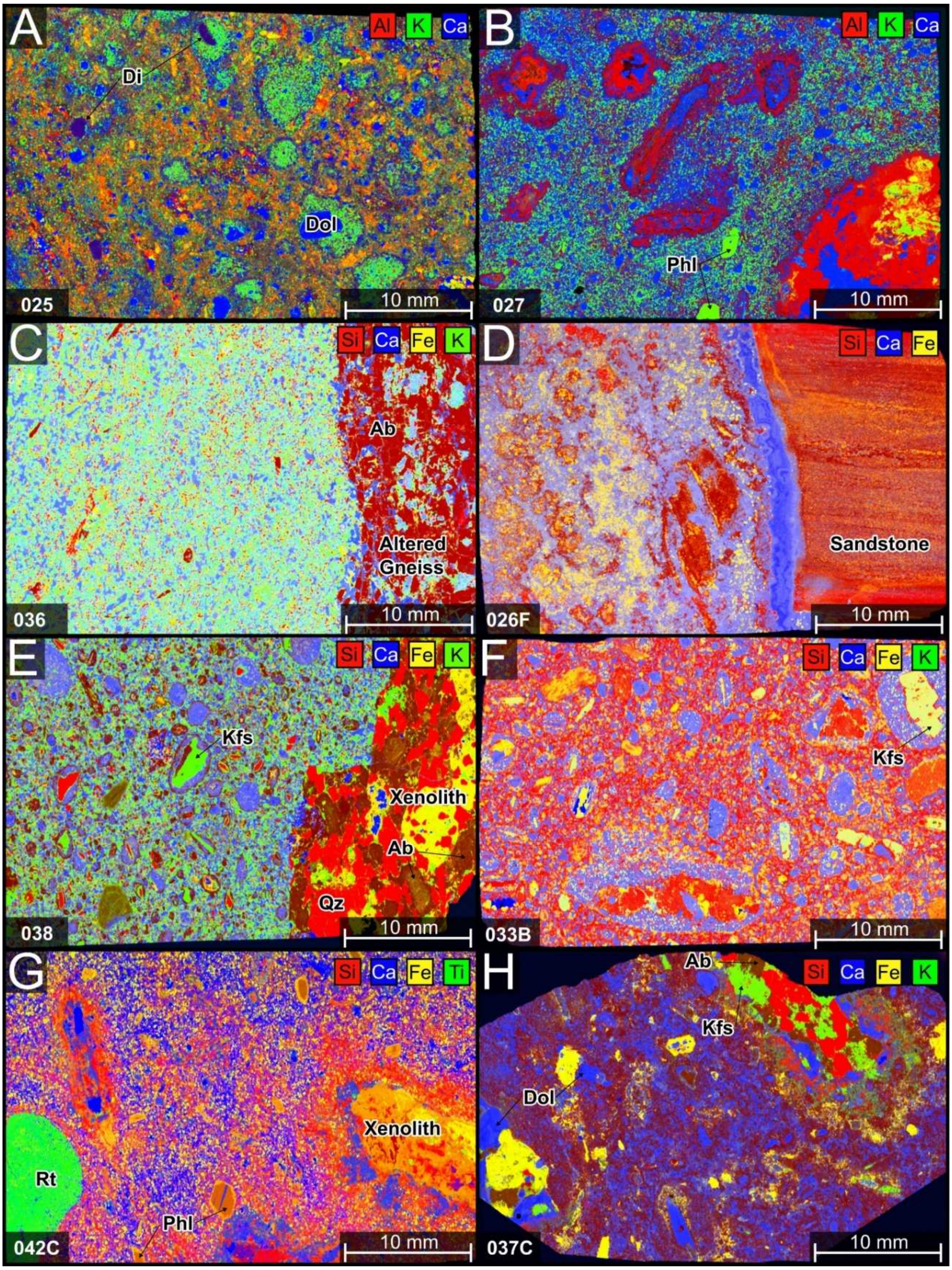

Figure 7. Selection of µXRF elemental mappings, showing KAP intrusives of various texture: A) Carbonate-poor matrix hosting diopside, dolomite and phlogopite macrocrysts, surrounded by K-enriched halos; B) Carbonate-rich and phlogopite phenocryst-bearing sample, hosting altered xenoliths now composed of albite, dolomite and some clinochlore; C) K-enriched matrix in contact with altered basement gneiss, composed of albite, dolomite and remains of K-feldspar; D) Altered xenoliths in a carbonate matrix in direct contact with Schwarzrand sandstone, with a later calcite veinlet (blue) along the contact; E) K-enriched matrix hosting lithic fragments (albite to K-feldspar) surrounded by a carbonate halo, and a large, altered basement gneiss xenolith; F) Lithic fragments (monomineralic, xenoliths) surrounded by carbonate halos in a Si-rich matrix; G) Rounded rutile macrocryst, phlogopite phenocrysts and altered xenoliths in a carbonate-bearing matrix; H) Variably altered granitic basement xenoliths hosted in a dolomite - albite matrix

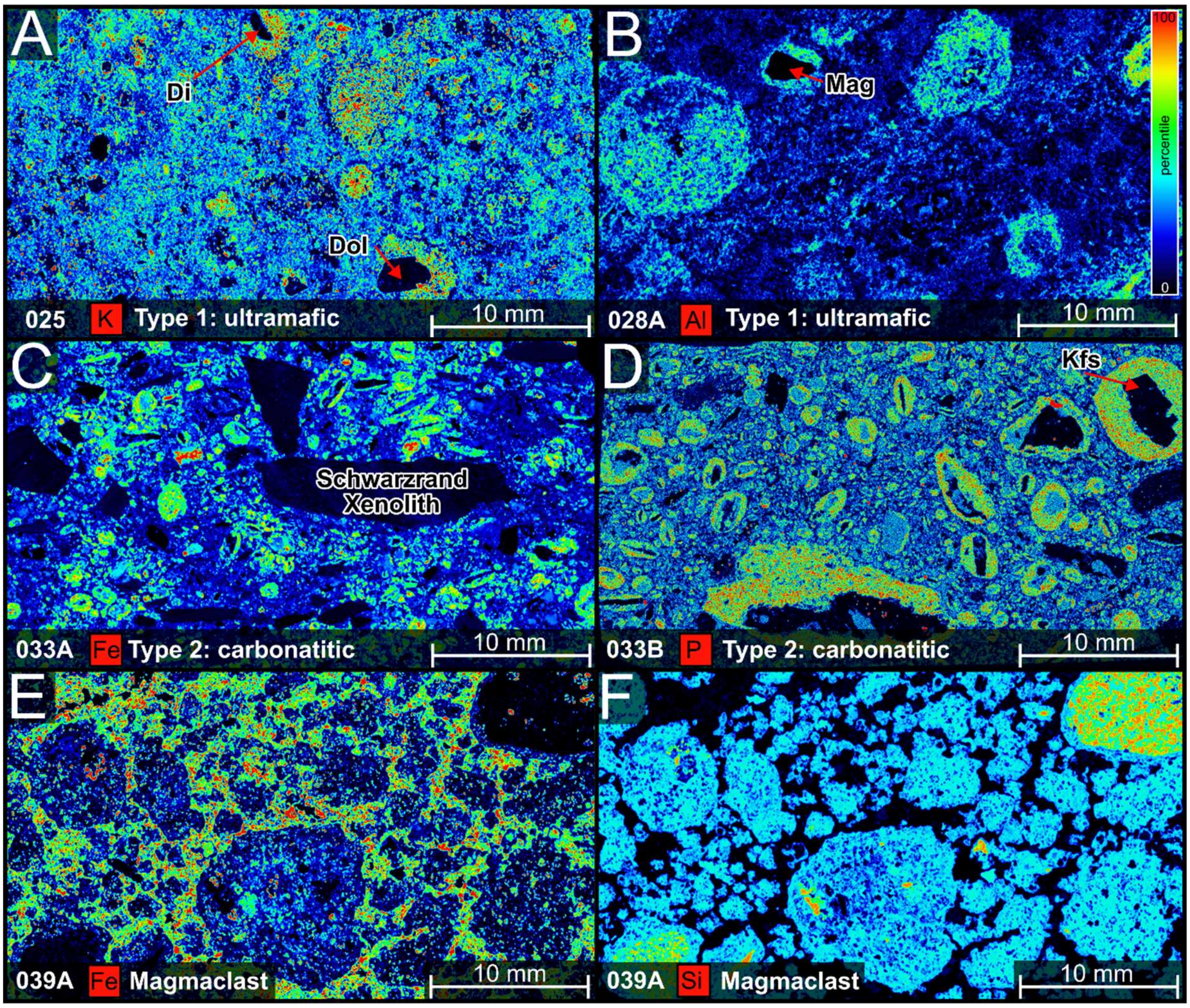

Figure 8. Representative intensity element mappings (percentile value distribution) of two types of pelletal lapilli, based on different halo compositions (derived from the globular sample GRB039A): A) Type 1 ("ultramafic") halos with elevated K concentrations; B) Type 1 with elevated Al concentrations; C) Type 2 ("carbonatitic") with elevated Fe contents. D) Type 2 with elevated P contents; E) Elevated Fe contents in the matrix surrounding the globules; F) Si contents, revealing rounded xenoliths with a rim and other, xenolith-free globules of similar composition

Phenocryst-Rich Varieties

Phenocrysts are mainly phlogopite (~ 1-5 mm), in some samples they make up up to 5 vol. % (Fig. 4I); commonly they have rounded rims due to alteration or partial resorption. The degree of alteration varies, but it is typically characterised by a dark band (Fig. 5C). This band contains subhedral magnetite, and albite surrounded by phlogopite (Fig. 9D). Small euhedral apatite crystals are present near the contact with unaltered matrix, still within the alteration zone (Fig. 9D).

Locally phenocrystic diopside is present, showing strong alteration especially along cleavage planes (Figs 5A and 7A). Surrounding the phenocrysts is later anhedral diopside and dolomite, as well as euhedral magnetite (Fig. 9C). These phenocrysts may be surrounded by globular structures with elevated levels of K, Ca, and Mn (Fig. 8A).

Other common components are carbonate “phenocrysts” of either dolomite or calcite, which may exhibit a superordinate crystal habit (e. g. pseudohexagonal). Unlike the matrix carbonates they are optically clear and composed of multiple equigranular mineral grains (Fig. 5B). They are either intergrown with opaque Fe-oxide or surrounded by an opaque seam. A singular, large (1.5 cm) titanium-rich macrocryst (Fig. 7G) comprises small, anhedral rutile crystals with interstitial calcite, albite and quartz with minor Ce-rich monazite, exhibiting a symplectitic texture. Phenocrysts of hornblende and a single kelyphitic garnet were documented by Schreuder (1975). Additionally, Winter and Rikhotso (1998) reported garnet, clinopyroxene, spinel, and ilmenite from the KAP, although they did not petrographic context or specific sample locations. It is to be noted that none of these minerals were identified in the current samples collected from the Garub valley.

Subvolcanic Breccia Characteristics (GRB027, 037C, 033)

In these xenolith-rich samples most clasts are derived from the gneissic basement (Figs 7B, E, G & H), but locally sandstone clasts derived from the Schwarzrand Subgroup are present (Figs 4B–C & 8C). Other xenoliths, e. g. mantle debris are absent, or at least untraceable. Additional common breccia constituents include xenocrysts, such as common alkali feldspar with partial albitisation, less frequent albite clasts, one angular magnetite as well as some undulous quartz clasts (Figs 8A & D). These clasts are commonly surrounded by a rounded halo or seam, which is distinguishable from the matrix by its contrasting colour (Figs 5D & 8A-D) or texture by displaying tangentially aligned lath-shaped albite or carbonate (more detail below). The less affected gneissic xenoliths are mostly composed of quartz and K-feldspar, with cracks filled by albite (Fig. 7H). Albite also appears to traverse around dolomite clasts, like the caulking of a sediment. More altered xenoliths appear to contain dolomite (dark-blue, Ca-mapping), likely replacing earlier constituents. In places, quartz and K-feldspar is still present, along with more common albite and dolomite (Figs 7B & E). Halos around these xenoliths are characterised by Fe-oxides and albite (Fig. 7H). Strongly altered gneissic xenoliths are composed of albite with interstitial dolomite seemingly replacing albite (Figs 7B & E). Smaller xenoliths have well-defined optical edges, but their elemental content transitions diffusely as albite crystallises beyond the original xenolith margins (Fig. 7B).

Globular Textural Features

Another distinctive feature of the diatreme samples is the common presence of globular textures (Figs 4B & G). They are spherical structures of hypabyssal material, reaching up to 100 mm in diameter, and referred to as pelletal lapilli, “well-rounded clasts consisting of an inner ‘seed’ particle with a complex rim, thought to represent quenched juvenile melt”, that formed within the diatreme (Gernon *et al*., 2012). Some of these pelletal lapilli contain xenoliths, while others contain xenocrysts; some samples contain phenocrysts derived from the basement gneiss (Fig. 7E). Several pelletal lapilli seem to lack seed fragments. The pelletal lapilli present in the Garub valley diatremes can make up more than 35 vol.% of the rock. The circular reaction rims have contrasting compositions to the matrix (Figs 7A & E-F) and were previously described as ankeritisation (Schreuder, 1975). Elemental mappings reveal that these seams are predominantly composed of Ca-carbonates and, to a lesser extent, Mg and Fe. Small apatite, rutile, and magnetite are present, along with larger hematite (bladed texture) and rutile farther away from the K-feldspar.

Based on these observations two types of pelletal lapilli can be distinguished. Type 1 lapilli occur in only two samples (GRB025, GRB028A). They have an "ultramafic" character, with macrocryst kernels or seeds of diopside, dolomite, and magnetite, surrounded by a halo of diopside, dolomite, and some euhedral (microcrystic?) magnetite, pyrite, and rutile (Fig. 13D). The elliptical halo is visible in qualitative µXRF element mappings of K or Al, which are elevated compared to the matrix (Figs 8A-B) More common are type 2 pelletal lapilli, which have a "carbonatitic" character. These commonly contain kernels derived from basement gneiss, and occur as xenoliths or xenocrystic K-feldspar, albite, or quartz, surrounded by a halo dominated by dolomite, with lesser albite, magnetite, rutile, and apatite (Fig. 13E). The halo is chemically distinct from the matrix, particularly in terms of Fe and P content, which are especially prominent in samples GRB033A and B (Figs 8C-D).

Sample GRB039A is notable for its unique texture, featuring globular structures differing from the pelletal lapilli (Figs 8E & F) and closely resembling magmaclasts, which are also referred to as globular (melt) segregations (Scott Smith *et al*., 2018). It contains two well-rounded, fine-grained xenoliths composed mainly of albite, quartz, rutile, and minor baryte and Fe-oxide. These xenoliths are encased in a fine-grained seam primarily made up of albite, with lesser amounts of rutile, dolomite, and minor apatite. In all other magmaclasts, xenoliths are missing, but their mineral composition is the same as that of the seam. All globules are embedded in a "matrix" composed of alternating layers of calcite and ankerite, which may grow euhedrally into former open spaces. One distinct section of the sample displays relatively euhedral mineral assemblages, which are typically smaller and unevenly dispersed (Fig. 9A-B).

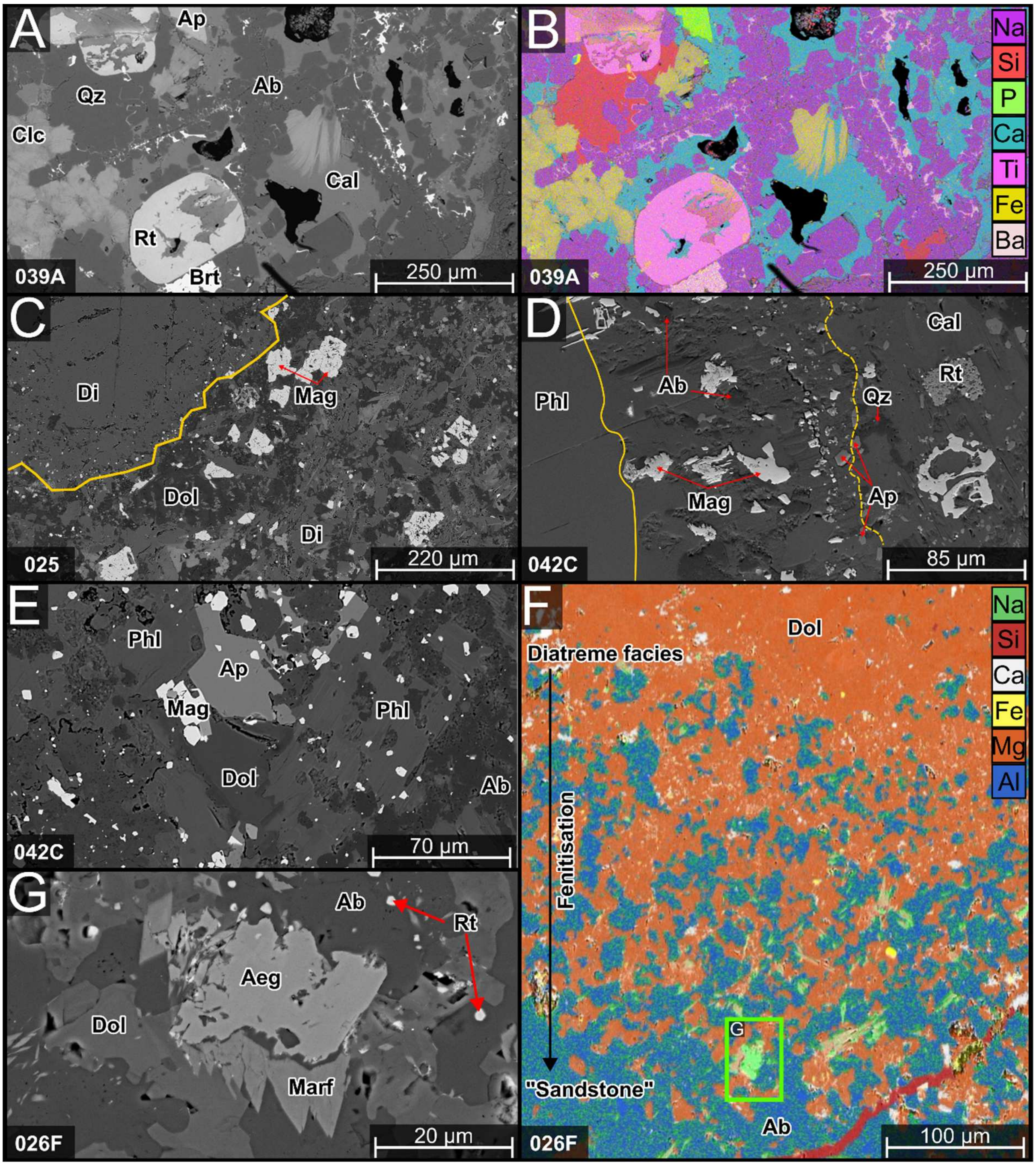

Figure 9. Selected back-scattered electron (BSE) images and EDX *(*energy dispersive X-ray) elemental mappings: A) BSE image of a euhedral assemblage comprising apatite, rutile, albite, and clinochlore, surrounded by interstitial calcite and quartz; B) Corresponding EDX mapping illustrating paragenetic relationships; C) Altered diopside phenocryst at the contact between diopside and its immediate surroundings; D) Phlogopite phenocryst with an alteration rim, as indicated by yellow lines; E) Close-up of the phlogopite-bearing matrix; F) EDX mapping of the direct contact between the diatreme facies and the Schwarzrand Subgroup, showing extensive fenitisation through a compilation of various elements: dolomite (orange), calcite (white), albite (greenish blue), and quartz (red). Location of the close-up BSE image is indicated by the green rectangle. G) Aegirine and magnesio-arfvedsonite surrounded by dolomite and albite

Wall rock contact alteration and fenitisation

To investigate contact relationships in detail and metasomatic interactions (fenitisation), multiple samples were selected from the contact between the Namaqua basement / Schwarzrand sandstone and the KAP intrusives (Figs 7C & D). Although metasomatic halos are not as prominent compared to intrusive carbonatite complexes, bleached basement is common a couple of metres around KAP diatremes. The contact between the diatremes and Schwarzrand sediments appears sharper than the contacts with the Namaqua basement. On sample scale, the Namaqua - KAP intrusive contact is characterised by elevated K contents within the aphanitic matrix, as indicated by elemental mappings (Fig. 7C). In contrast, the basement or basement-derived xenoliths exhibit K-feldspar variably replaced by albite or, in some cases, consist solely of albite (Figs 7B & C). This implies sodium enrichment in the wall rock and a corresponding potassium enrichment within the diatremes. Sample GRB026F shows a sharp contact between a dyke and Schwarzrand sandstone (7D). BSE imaging and EDX mapping (Fig. 9F) reveals that the diatreme at the top of the image, composed of dolomite (orange) and interstitial calcite (white), transitions to albite-dominated sandstone (blue) at the bottom with green spots of aegirine and a quartz vein (red). High resolution BSE imagery reveals the presence of aegirine and magnesio-arfvedsonite with a characteristic wedge shape (Fig. 9G), and sodic metasomatism emanating from the intruding dyke. Scattered, relatively small rutile is also present.

Whole Rock Analysis and Geochemistry

For this study, 35 whole-rock analyses were conducted on selected samples from the Garub valley. The results of these analyses are presented in appendices 3-5. Please note that the diatreme facies samples commonly contain clasts and xenoliths of various lithologies, which implies significant contamination of the original magma. Therefore, all whole rock data should be interpreted with this potential contamination in mind.

Major Elements

The binary diagrams in Figure 10 reveal several notable features. The samples from the Garub valley closely align with those from the broader KAP analysed by Schreuder (1975). It is interesting that the fenitisation of the gneissic basement is also evident from the chemical data. Some basement samples show a loss of SiO_2 (up to 20 wt.%) and Fe_2O_3, concomitant with a gain of CaO and Na_2O. The behaviour of the alkalis is particularly interesting as it complements earlier insights into the character of the fenitisation, with two distinct tendencies observed: the basement gneiss becomes enriched in Na_2O and depleted in K_2O (almost 4 wt.%; Fig. 10C-D), clearly showing a sodic fenitising character. Similarly, one of the two siltstone samples follows this gain and loss trend.

Analysed KAP rocks vary significantly in K_2O content and do not accurately plot within the ultramafic lamprophyre field as defined by Rock (1986; Fig. 10D). The distinction between ultramafic and calc-alkaline lamprophyres can be made using TiO_2 content, with a threshold of 2.5 wt.% (Rock, 1986). Nearly all diatreme samples fall just above this value, which is characteristic of ultramafic lamprophyres.

When compared to similar occurrences of diatreme-hosted ultramafic intrusives, such as Aillik Bay (Canada; Tappe *et al.*, 2006) and Gross Brukkaros (Walter *et al.*, 2023), or carbonatites and aillikites from the Batain Nappes diatremes (Oman; Nasir *et al.*, 2011), the chemistry of the analysed rocks most closely resembles aillikites and damtjernites. There is a notable overlap in SiO_2 vs CaO and SiO_2 vs TiO_2 ratios (Figs 10A & F), but a significant discrepancy in the Al_2O_3 vs MgO bivariation (Fig. 10G). The ultramafic lamprophyre (UML) suite, including some primary silicocarbonatites from the Beara Peninsula (Ireland; Moore *et al.*, 2022), also shares similar compositional traits. The diatreme or dyke-hosted carbonatites and the KAP intrusives exhibit a close chemical affinity, more particularly overlapping with Garub valley samples of lower SiO_2 content.

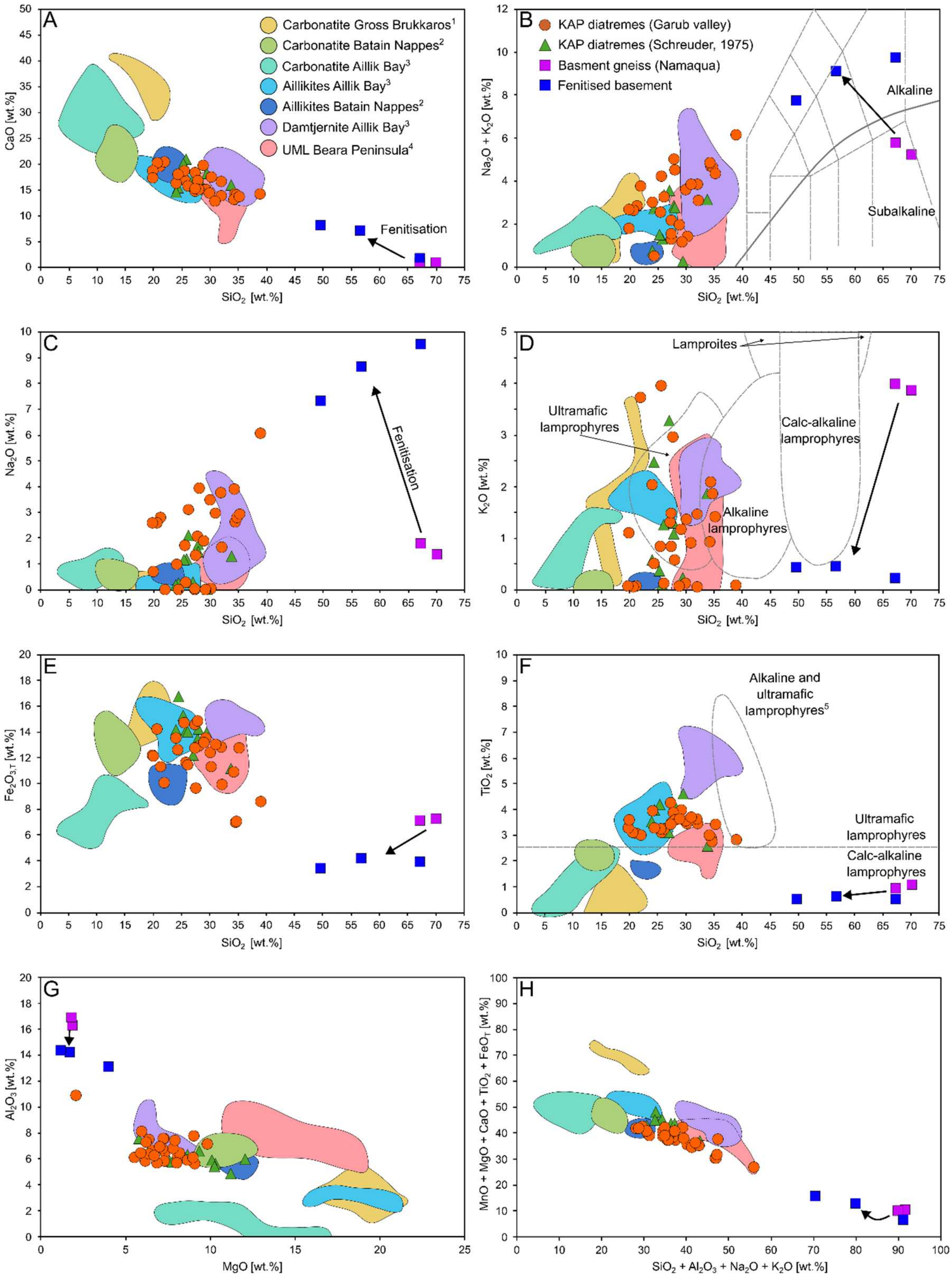

Figure 10. Binary plots illustrating the composition of present KAP samples, previous KAP data (Schreuder, 1975), basement gneiss, fenitised basement, Gross Brukkaros carbonatitic diatremes (Walter *et al*., 2023), carbonatites/aillikites from Batain Nappes diatremes (Nasir *et al*., 2011), carbonatites, aillikites and damtjernite from Aillik Bay (Tappe *et al*., 2006) and silicocarbonatite and lamprophyre from Ireland (Moore *et al*., 2022). Arrows indicate chemical changes due to fenitisation. A-F) Major element vs SiO_2 plots: B) classical TAS discrimination, D) discrimination after Rock (1986); F) mafic and calc-alkaline distinctions after Rock (1986) / alkaline and ultramafic lamprophyre fields after Krmíček and Chalapathi Rao (2022); G) Al_2O_3 vs MgO plot; H) plot of elements compatible in carbonatite vs carbonated-silicate melts

Differences within the KAP intrusive rocks based on factors such as emplacement mode (diatreme, dyke, or sill), country rock type, texture, and appearance were considered to identify chemical groupings, but this approach has not been particularly successful. To compare the Garub intrusives with other ultramafic rocks worldwide, a database comprising 3857 carbonatite analyses (DIGIS Team, 2025), 1821 kimberlite samples, and 324 ultramafic lamprophyres (Giuliani *et al*., 2025) was used. The analysed KAP diatreme samples, with an average of ca. 28.1 wt.% SiO_2, are akin to the average compositions of ultramafic lamprophyres and kimberlites, while carbonatites typically contain less than 10 wt.% SiO_2.The average CaO content of 16.4 wt.% is generally higher than that of ultramafic lamprophyres and kimberlites, which hover around 10 wt.%, while in carbonatites Ca typically is the most abundant element. Na_2O contents of up to 6 wt.% are relatively high, and are usually found only in extrusive carbonatites such as Oldoinyo Lengai (Tanzania), rarely in ultramafic lamprophyres or kimberlites. Potassium contents, with an average of ~1.2 wt.%, are scattered and fall within the range of other ultramafics.

Fe content (Fe_2O_3total) is slightly higher than in kimberlites, with an average of ~11.9 wt.%. TiO_2, averaging 3.4 wt.%, is even more elevated compared to kimberlites, and also unusually high relative to carbonatites. In contrast, MgO, averaging 7.2 wt.%, is very low compared to kimberlites and ultramafic lamprophyres, but falls within the range of carbonatites. Other major elements, such as Mn_2O_3 (average of 0.3 wt.%) and P_2O_5 (average of 1.2 wt.%), and loss on ignition (average of 20.5 wt.%), are detailed in appendices 3-5.

The classical definition scheme for carbonatites proposed by Gittins and Harmer (1997) was employed, given the significant carbonate component in the magmatic rocks. This approach indicates that the KAP rocks are ferrocarbonatites to ferruginous calcio-carbonatites. When considering the potential influence of other Ca-, Mg-, or Fe-bearing minerals, such as Fe oxides or phlogopite, the data points do not represent the carbonate fraction. Thus, it is assumed that they fall a bit farther away from the FeO/MnO end member, between the ferruginous calcio-carbonatite and magnesio-carbonatite field, only taking the carbonate composition into account.

As the KAP rocks have been previously described as ultramafic lamprophyres or alnöitic tuffisites, a second classification scheme after Rock (1986) is deemed appropriate (Fig. 11A). This scheme is based on MgO, FeO_T, and Al_2O_3 content ratios and places the Garub rocks within the alnöite and aillikite fields. Other occurrences of UMLs and carbonatite plot nearby, but have higher MgO contents, although they still lie within the above fields (Fig. 11A).

Trace Elements

Primitive mantle-normalised REE patterns (Fig. 11B) demonstrate that the Garub intrusives are compositionally similar, though slightly enriched in LREE relative to the REE-depleted Nama Group host rocks, which exhibit a negative Europium (Eu) anomaly. This anomaly also appears in the basement gneiss and its fenitised equivalent. The unfenitised basement is richer in HREE than the KAP suite, while one fenite sample is LREE-enriched but nearly HREE-devoid. Calcite carbonatites from Dicker Willem show similar REE trends, with Garub valley samples overlapping the lower part.

On a Sm vs La/Yb plot, these samples lie just above the UML field (Rock, 1986), due to elevated Sm levels (Fig. 11C). Sm/Yb vs La/Yb trends align with partial melting (~7%) of carbonated garnet peridotite (Fig. 11D), diverging from pure garnet or spinel peridotite sources with lower Ta/Yb. The Ce/Pb vs Sm/Nd plot (Fig. 11E) suggests crustal assimilation during melt ascent. High Ce/Pb implies an asthenospheric source; lower values indicate upper/middle crustal contamination. While such trace element ratios are typically applied to basaltic systems, their application to UMLs yields useful, though simplified, insights into mantle processes. Radiogenic isotope studies remain essential for definitive source interpretations.

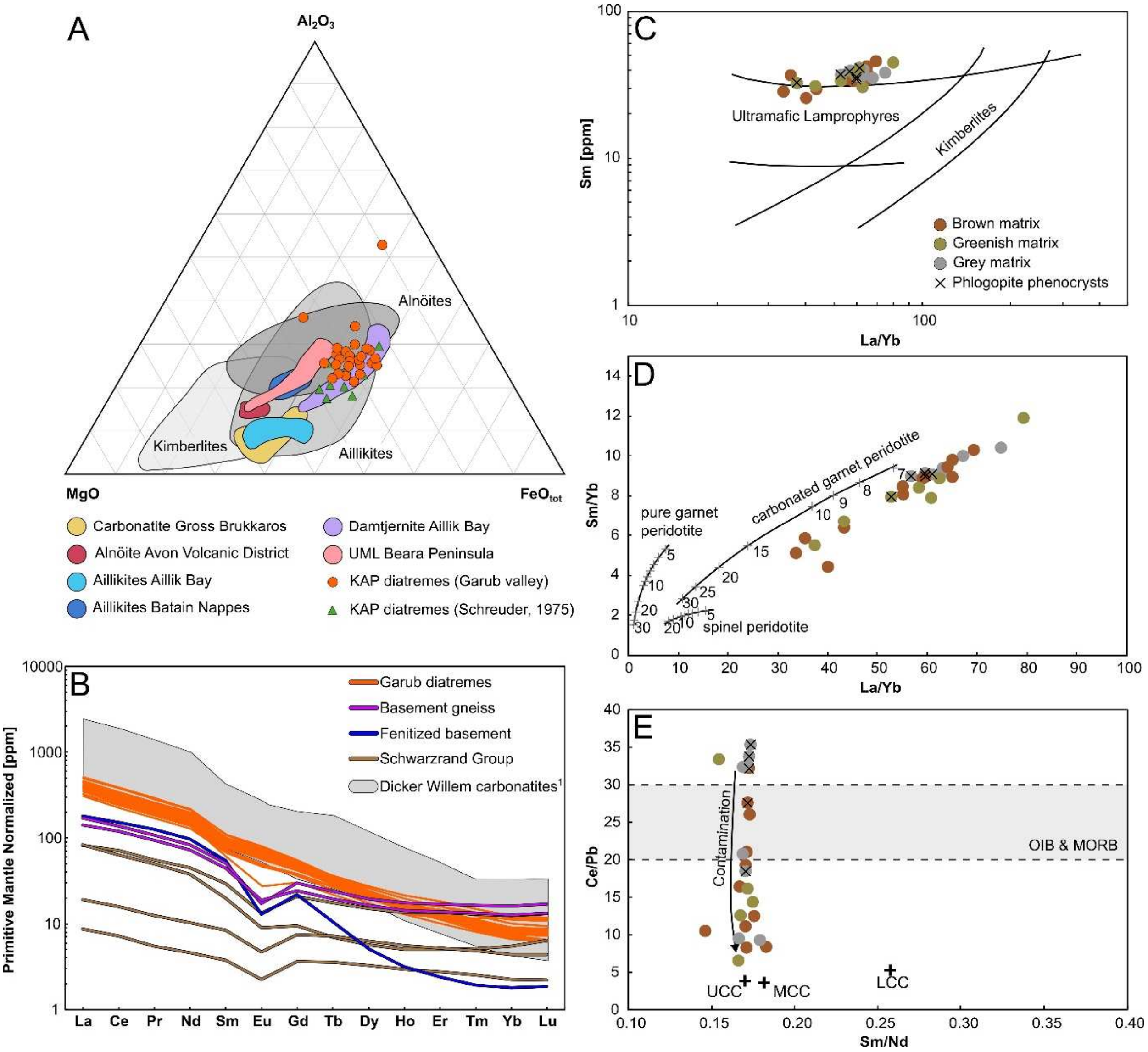

Figure 11. A) Classification for kimberlites, aillikites and alnöites following Rock (1986); comparative data are from carbonatitic diatremes from Gross Brukkaros (Walter *et al*., 2023), alnöites from the Avon Volcanic District (Shavers *et al*., 2016), aillikites and damtjernite from Aillik Bay (Tappe *et al*., 2006), aillikites from Batain Nappes diatremes (Nasir *et al*., 2011) and silicocarbonatite and lamprophyre from Ireland (Moore *et al*., 2022); B) Primitive mantle-normalised rare earth element (REE) plot after Sun and McDonough (1989) of the Garub intrusive suite including Namaqua basement gneiss, fenitised basement, and Nama Group host rocks (brown). For reference, values for the Dicker Willem calcite carbonatites (grey) are shown, representing a classical REE-barren carbonatite (unpublished data); C) Sm vs La/Yb plot after Rock (1986) showing fields for kimberlites and ultramafic lamprophyres; D) Sm/Yb vs La/Yb plot showing melting curves calculated for spinel peridotite, garnet peridotite and carbonated garnet peridotite, with numbers representing the degree of partial melting (adapted from Yu *et al*., 2015); E) Sm/Nd vs Ce/Pb plot showing ranges of typical OIB and MORB Ce/Pb ratios, and depleted mantle ratios (Hofmann *et al*., 1986), together with average upper continental crust (UCC), middle continental crust (MCC) and lower continental crust (LCC) (from Rudnick and Gao, 2003; diagram adapted from Yu *et al*., 2015)

Stable Isotopes

Carbon and oxygen isotope data of the Garub valley samples, along with six measurements from other KAP occurrences, are plotted together with data from various kimberlites, carbonatites, and ultramafic lamprophyres (Fig. 12). The Garub valley diatremes develop towards heavier isotopic ratios ($\delta^{18}O$, 15.1 to 19.5; $\delta^{13}C$, -4.1 to -0.84 ‰; Appendix 6) that align well with the Rayleigh (high temperature) fractionation or metasedimentary contamination trend (Deines, 1989). Data for Nama Group carbonates show characteristic values for limestone with an average of around 23.0 ‰ ($\delta^{18}O$) and 1.6 ‰ ($\delta^{13}C$) situated atop of this trajectory (Ries *et al*., 2009). Isotopic data for the gneissic basement is lacking, but $\delta^{18}O$ values for granitic to gneissic basement rock (e. g. Archaean crust) are generally around 10 ‰, and are unlikely to cause contamination (Harris *et al*., 2015, and references therein). The studied samples also show heavier carbon and oxygen isotopes compared to primitive igneous carbonatites (PIC; Taylor *et al*., 1967; Keller and Hoefs, 1995), to which aillikites from Aillik Bay (Canada) and some unevolved carbonatites belong (Fig. 12). The Garub valley samples display an increase of up to 10‰ in $\delta^{18}O$ and up to 4‰ in $\delta^{13}C$ relative to aillikite and some carbonatites. More evolved carbonatites (fractionated) as well as kimberlites from Udachnaya East (Siberia) and damtjernites from Chuktukon (Siberia), share a similar range of isotopic values. One measurement from the Gross Brukkaros carbonatite falls between the Garub valley diatremes and the broader KAP data, exhibiting relatively heavy $\delta^{18}O$ (> 25 ‰) and low $\delta^{18}C$ (< -4 ‰) values. These samples potentially follow the low temperature/hydrothermal alteration trend or the degassing trajectory away from the Garub valley trend, probably because of the hypabyssal emplacement mode and subsequent degassing and alteration. Sample GRB039A (globular textures) from the Garub valley shares these characteristics with the KAP samples.

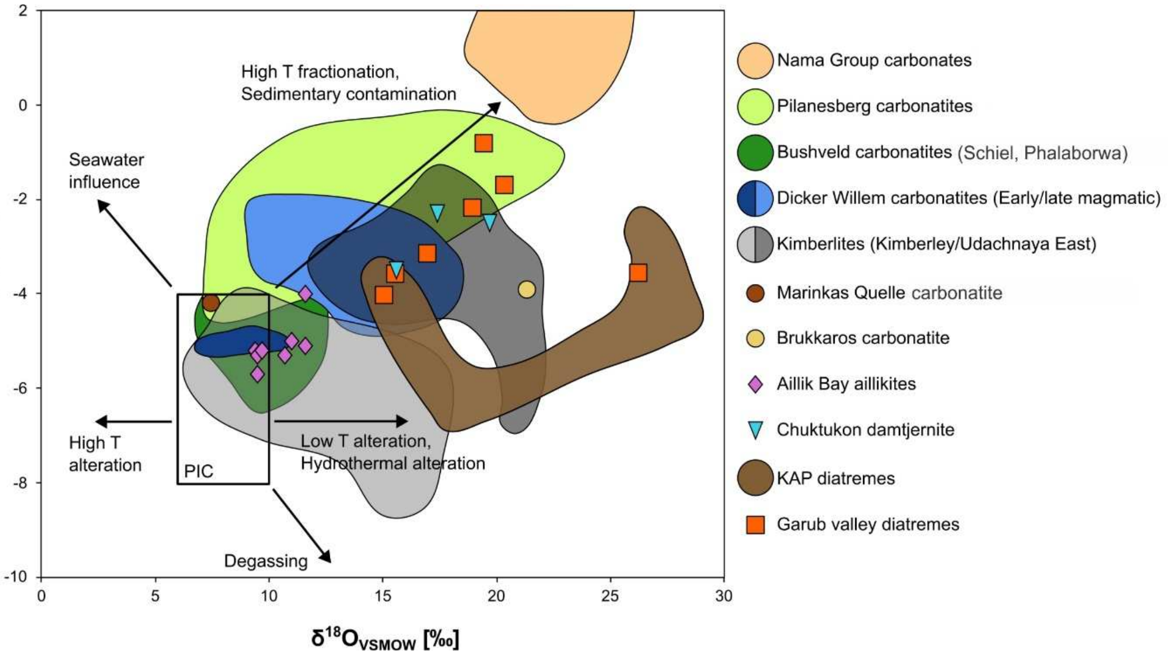

Figure 12. Carbon and oxygen isotope diagram displaying the Primary Igneous Carbonatite (PIC) field, based on Taylor *et al*. (1967) and Keller and Hoefs (1995), with arrows indicating processes that shift isotope ratios, following Deines (1989); also shown are data from the Nama Group sediments (Ries *et al*., 2009), Marinkas Quelle carbonatite (Horstmann and Verwoerd, 1997), Brukkaros carbonatite (Horstmann and Verwoerd, 1997), Pilanesberg carbonatites (Glenover, Nooitgedacht, Goudini, Kruidfontein, Bulhoek, Tweerivier, Stukpan, Spitskop, and Derdepoort; Horstmann and Verwoerd, 1997), Bushveld carbonatites (Schiel, Horstmann and Verwoerd, 1997; Phalaborwa, Munro and Harris, 2023), Dicker Willem (Reid and Cooper, 1992), kimberlites (Giuliani *et al*., 2014), aillikite from type locality Aillik Bay (Tappe *et al*., 2006), damtjernite from the Chuktukon Complex (Siberia; Doroshkevich *et al*., 2019) for comparison with the Kainab Alkaline Province (KAP) and Garub valley diatremes.

DISCUSSION

Classification of the Garub valley diatremes: kimberlites, ultramafic lamprophyres, or carbonatites?

The KAP diatremes have been variously described as alnöitic tuffisites and lamprophyric carbonate rocks (Schreuder, 1975), carbonatites of uncertain affinity (Verwoerd, 1993), olivine melilitites (Spriggs, 1988), or parakimberlite (Winter and Rikhotso, 1998), underscoring the petrological and genetic complexity of these bodies. The common occurrence of phlogopite and less frequent diopside macrocrysts are characteristic of ultramafic lamprophyres as well as of kimberlites. In addition, although olivine has not been found in the studied samples, it may have been originally present, as indicated by pseudomorphic replacements by chlorite (Fig. 5E; Schreuder, 1975). The reported mineral data of garnet, spinel, clinopyroxene and ilmenite (Winter and Rikhotso, 1998), and a described kelyphitic garnet and rare augite (Schreuder, 1975) point towards mantle derived rocks for the KAP, although in the Garub valley samples none of these minerals have been observed apart from one rutile macrocryst and some clinopyroxene (Fig. 7G). The absence of these mantle-derived macrocrysts is atypical for mantle derived rocks (Tappe *et al*., 2005). Especially the presence of abundant interstitial quartz (matrix) throughout most samples complicates their proper classification and indicates that the Garub valley diatremes do not represent pristine mantle-derived rocks, but have undergone modification/contamination.

One distinguishing feature is the presence of local groundmass clinopyroxene in the samples, which excludes their classification as kimberlites or ultrapotassic orangeites (Tappe *et al*., 2005). Furthermore, the studied samples also are chemically distinct from kimberlites, as they display, on average, a relatively low Mg content of 7.2 wt.%, while kimberlites are generally richer in this element.

The Al_2O_3–FeO–MgO discrimination diagram (Fig. 11A; Rock, 1986) suggests that the KAP rocks are chemically related to ultramafic alnöites or aillikites. According to Tappe *et al*. (2005), three end members describe the petrographic and compositional continuum of ultramafic lamprophyres: alnöite (characterised by essential groundmass melilite), aillikite (characterised by essential primary carbonate), and damtjernite (characterised by essential groundmass nepheline and/or alkali feldspar). The KAP intrusives exhibit characteristics of both aillikite and damtjernite, being carbonate-rich and containing abundant albite/oligoclase. Evidence of melilite is solely based on the assumption that lath-shaped carbonates or feldspars are pseudomorphs after melilite (Schreuder, 1975). As no relics of melilite were found during this study, and laths of calcite or dolomite can be primary in carbonatites and aillikites (Tappe *et al*., 2006), the classification of the KAP diatremes as alnöites is rejected here. Similarly, in the Gardar alkaline igneous province (Greenland), the interpretation of carbonates as pseudomorphs after melilite has been questioned, leading to the rejection of a prior classification as alnöites (Upton *et al*., 2006).

Due to intense interaction and modification during emplacement, likely influenced by the presence of silicic xenoliths and other lithic fragments, the original composition of these rocks is cryptic. When accounting for significant Si and Al input from contamination and considering an originally higher Na content (subsequently depleted by fenitisation), an original carbonatitic character appears plausible. Based on µXRF mappings, a primary carbonate content of 30–50 vol.% is suggested, which may have been even higher if xenocrystic material is excluded. This would classify most samples as carbonatites, while the prevalence of dolomite over calcite and the high silica content (>20 wt.% SiO_2) further classifies these rocks as dolomitic silicocarbonatites (Le Maitre, 2002; Mitchell, 2005; Yaxley *et al*., 2022; Tappe *et al*., 2025).

However, due to their ultramafic character, particularly the presence of phlogopite macrocrysts, classification as aillikite-damtjernite (transition) is also possible. Since damtjernites have been considered gangue equivalents to carbonatites (Kapustin, 1981), the authors interpret the Garub valley rocks as hypabyssal dolomite silico-carbonatites with a distinguished UML affinity. A smooth transition between these rock types is possible.

Origin of Textures and their Implications

Magmaclasts as evidence for carbo(hydro) thermal fluids?

These segregations can resemble pelletal lapilli in their petrographic features, but are generally coarser and often lack a macrocrystal core (Clement, 1982). Where abundant, they give the rock a pseudo-conglomeritic appearance (Fig. 3H). They are believed to form due to surface tension in boiling magma within near-surface hypabyssal environments, as proposed by Clement (1982) and Mitchell (1986). The term "globular segregations," initially introduced by Clement and Skinner (1985), has evolved into the descriptive term "magmaclasts", now widely accepted (Webb and Hetman, 2021). The origin of these textures, involving the interplay of explosive emplacement, magma fragmentation, and physical aspects such as pipe or diatreme geometry, is diversely discussed and interpreted (Scott Smith *et al*., 2018; Webb and Hetman, 2021 and references therein).

The observed globular texture in the samples closely resembles magmaclasts, with uniform rims encompassing rounded xenoliths to distinguish them from resorbed xenoliths or breccias. Additionally, the curvilinear edges with sharp transitions to the calcite and siderite matrix (as seen in Figs 8E-F) and the abundance of vesicles (shown in Figs 9A-B) point to a magmaclastic origin rather than a brecciated one. The magmaclasts are surrounded by euhedral calcite and interposed bands of ankerite, thought to have precipitated from a carbo(hydro)thermal fluid, either derived from a late pulse associated with the earlier ascending melt or, more plausibly, exsolved from the freshly contaminated melt. The mineral assemblage of the magmaclasts (Figs 9A-B) is interpreted to consist of microcrysts of apatite, rutile, and magnetite, surrounded by calcite, albite, and clinochlore with some baryte, which are all minerals commonly associated with hydrothermal regimes. However, as these magmaclasts are separated from the matrix and differ in containing silicate phases, they represent a transitional stage between hydrothermal and magmatic conditions. This could arguably be labelled as the brine-melt stage (Walter *et al*., 2021). Evidence pointing towards a hydrothermal regime are also the elevated δ^{18}O values of the carbonates, which is attributed to the common dolomite and ankerite matrix (Fig. 12). Quartz cannot form in carbonatites under typical magmatic conditions (>400°C) due to the low silica activity in carbonatitic systems at high temperatures (Massuyeau *et al*., 2015). However, at lower temperatures, such as those found under hydrothermal conditions, silica buffering ceases, allowing quartz to become stable (Yaxley *et al*., 2022). It is believed that during the adiabatic cooling of the brine-melt upon partial vaporisation (eruption), silica buffering decreases abruptly, facilitating the immediate formation of quartz (Walter *et al*., 2023).

Pelletal lapilli as evidence for two types of melt

Pelletal lapilli are primary magmatic constituents, not rounded xenolithic clasts, and are characteristic of diatreme rocks, indicative of diatreme environments (Mitchell, 1995). Although originally described in kimberlites, they are also present in melilitites, orangeite, or, more rarely, in carbonatite diatremes (e. g. Carnevale and Zanon, 2024). Rocks containing pelletal lapilli derive from CO_2–rich magmas (Mitchell, 1995) and are believed to form by rapid expulsion of dissolved volatiles (Clement, 1982) or by interaction with groundwater (Mitchell, 1986). As suggested by Gernon *et al*. (2012) their formation can be explained by gas jets caused by strong degassing, lifting and coating nearby particles with a low-viscosity melt (Fig. 13).

In the studied rocks, the seed materials are commonly alkali feldspar (probably derived from basement gneisses), but also xenoliths (Figs 7E-F). Some kernels appear to have been altered to carbonate, veiling their original composition. The rims of the kernels vary, but tiny (<50 µm) dolomite, rutile, magnetite, and apatite crystals are present throughout, indicating high-temperature formation (Prokopyev *et al*., 2023). The absence of accretionary lapilli and glassy or bread-crust surfaces suggests high-temperature, mostly "dry" eruption conditions (Lloyd and Stoppa, 2003), pointing to the rapid expulsion of dissolved volatiles rather than an interaction with groundwater. This is in accordance with the stable isotope data, in which there seem to be no evidence of alteration due to meteoric water, but rather evidence pointing towards degassing (Fig. 12).

Two distinct types of pelletal lapilli,

with distinct mineral seeds and “halos” have been encountered. Accordingly, two discrete environments are assumed for their formation, differing both in location and melt composition. The location, in terms of relative depth within a diatreme system (Fig. 13A), varies as type 1 pelletal lapilli are found in xenolith-barren samples. This suggests either a sub-explosive level (root zone) or, more likely, a less violent emplacement lacking strong brecciation and associated CO_2 exsolution. This aligns with the differing types of kernels, interpreted to be mantle-derived diopside and magnetite, along with dolomite probably replacing original olivine and diopside (Figs 5A-B, 7A, 8A-B & 13D). Thus, type 1 pelletal lapilli indicate an essentially ultramafic and uncontaminated silicate melt (no basement fragments present), allowing the formation of later diopside around diopside macrocrysts.

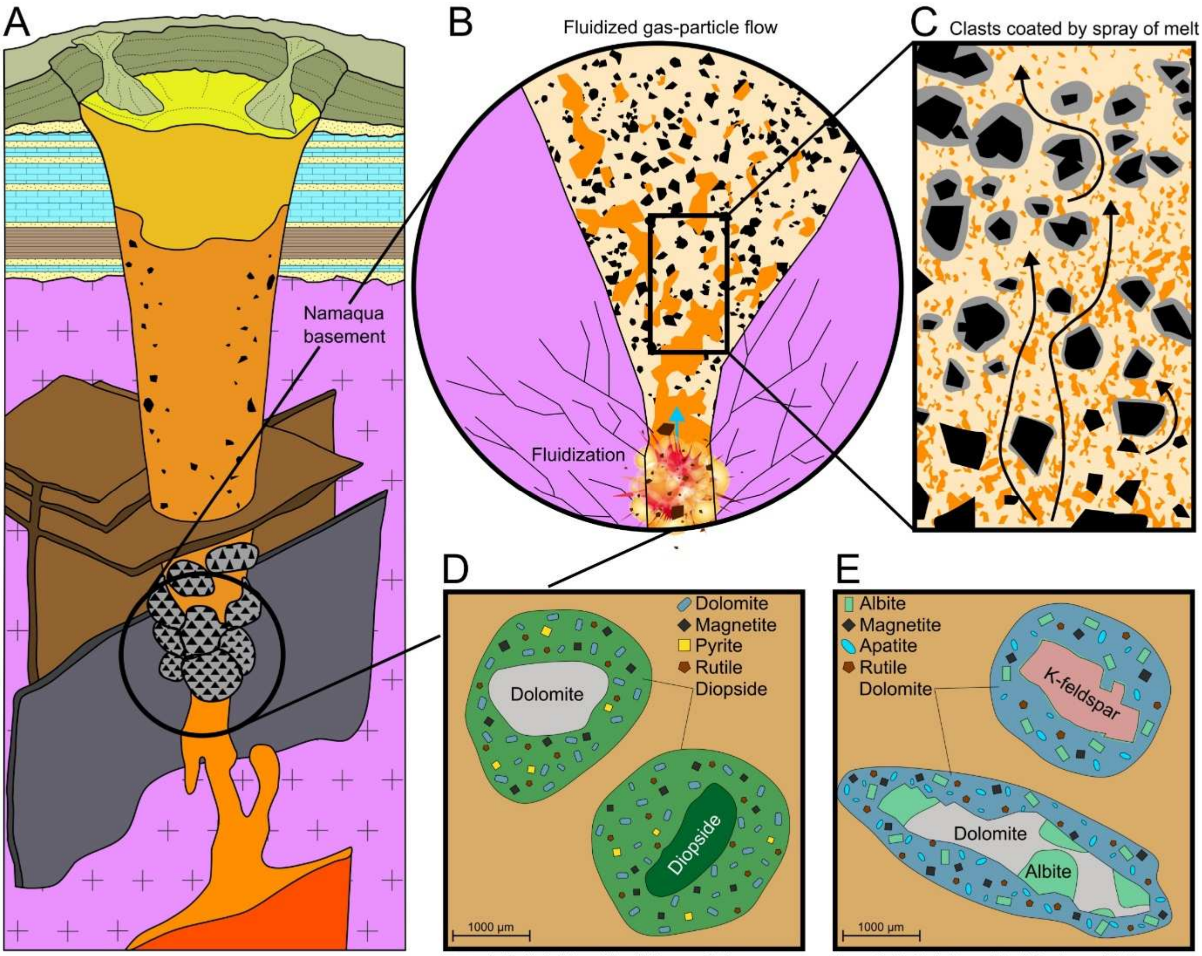

Type 1 Pelletal Lapilli - "Ultramafic"   Type 2 Pelletal Lapilli - "Carbonatitic"

Figure 13. Schematic illustration depicting the formation of pelletal lapilli within diatremes in the Garub valley: A) Cross-section of a diatreme adapted from Mitchell (1986) reflecting the local geology; B) Closer view of the lower diatreme facies, illustrating the explosive emplacement of a mingled, CO_2-exsolving melt (fluidised gas-particle flow); C) This process leads to the formation of pelletal lapilli, which are lithic fragments coated by sprayed melt-particles during their turbulent, fluidised ascent. D) Type 1 ultramafic pelletal lapilli, consisting of a phenocryst kernel surrounded by a halo rich in diopside and dolomite, with minor amounts of magnetite, pyrite, and rutile (sketch based on sample GRB025); E) Type 2 carbonatitic pelletal lapilli featuring xenolith and xenocryst kernels from the surrounding Namaqua basement, encased in a halo primarily composed of dolomite and albite, along with apatite, magnetite, and rutile (sketch based on sample GRB033B)

Type 2 pelletal lapilli are typically found in samples that are rich in basement fragments, which almost all serve as seeds (Figs 5D, 7E-F, 8C-D, 13E). Xenoliths from the Schwarzrand Subgroup show no reaction, likely because they were a late addition to the already formed pelletal lapilli. The melt had probably already reacted with these xenoliths (resorption, Fig. 15), overcoming the chemical gradient between the ultramafic melt and the felsic xenoliths. Consequently, the emplacement level of this sample should be significantly above the site of explosion (also indicated by the relatively small size of pelletal lapilli). In contrast, the pelletal lapilli with larger and solely gneissic xenoliths/xenocrysts with halos, probably solidified at deeper levels closer to the explosion. This variation is likely due to different velocities of the kernels being sprayed by the melt, with larger particles moving upward more slowly, allowing for size-based sorting within a single diatreme. Since halos of type 2 pelletal lapilli are practically devoid of silicate minerals (apart from minor albite), the melt spraying the lithic fragments probably was of a carbonatitic character. Thus, these halos provide evidence of a carbonatitic melt before intensive contamination or leaching of the basement introduced significant amounts of Si, Al, and other felsic-typical elements.

In summary, these two pelletal lapilli types indicate the presence of two distinct melts that formed the Garub intrusives. As the matrices of most samples are quite similar, they are believed to represent the resulting, heavily contaminated melt after the explosive emplacement level, probably affected by successive hydrothermal fluids. This process resulted in relatively uniform whole-rock compositions throughout the numerous intrusives of the Garub valley.

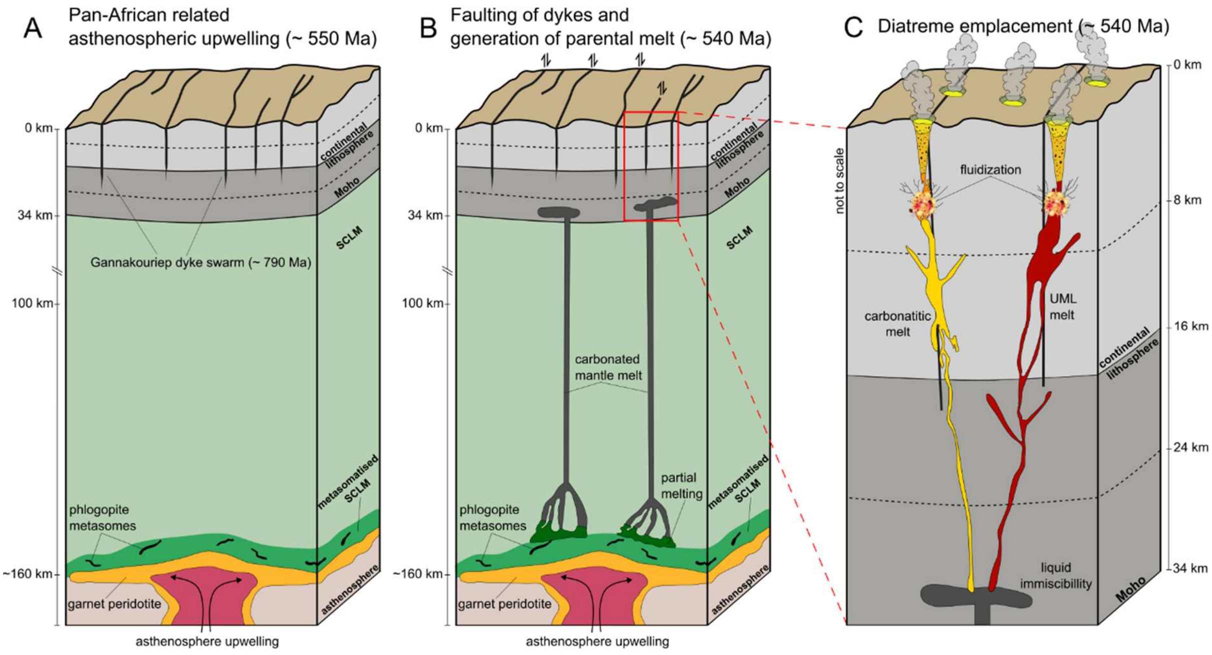

Figure 14. Schematic illustration depicting the assumed stages leading to diatreme formation in the Garub valley. The process is shown by means of cross-sections extending to the asthenosphere (not to scale), including asthenospheric upwelling, phlogopite metasomes, and partial melting: A) llustrates the Pan-African related asthenospheric upwelling; B) Partial melting generates a mantle-derived carbonated peridotite melt ascending through the SCLM (subcontinental lithospheric mantle).; C) Further ascent of a now immiscible mantel melt (carbonatite - yellow; UML - red) along pre-existing faulted dykes to shallow crustal levels and subsequent fluidisation, resulting in diatreme eruptions in the Garub valley

Deciphering the Magmatic Evolution and Origin

Mantle Source of the Primary Melt?

At Garub, primitive ultramafic lamprophyres (type 1 pelletal lapilli) likely represent carbonated mantle melts from depleted sources. At adiabatic temperatures, carbonatites cannot form in the asthenosphere, as the mantle adiabat exceeds the solidus of carbonated peridotite by 200–300 °C (Dasgupta *et al*., 2013). At 5–7 GPa, carbon exists as diamond, graphite, or alloy—not carbonate. During upwelling, garnet releases Fe^{3+}, oxidising carbon to CO_2, lowering the solidus by ~400 °C and producing carbonated silicate melts (Walter, 1998; Schmidt *et al.*, 2024). These melts are therefore carbonated silicates, not pure carbonatites. To produce the chemical characteristics observed in the Garub diatremes (high Ti, Fe, and Na) and explain the presence of phlogopite and diopside phenocrysts, partial flux-melting of phlogopite-ilmenite metasomes within the cratonic mantle is assumed (Pilbeam *et al.*, 2024). Accordingly, Nd-Hf isotope data from Labrador aillikites result from interactions between an asthenospheric carbonate-rich silicate melt and melts from K-rich metasomes in the cratonic mantle lithosphere (Tappe *et al.*, 2008). Evidence pointing towards a garnet peridotite mantle source includes the reported presence of a garnet phenocryst with a kelyphitic rim (Schreuder, 1975), believed to form around mantle garnets during their ascent (Obata, 2011). Limited mineral data report lherzolitic garnets, garnet-peridotite derived clinopyroxenes and mantle-derived spinels from the Kainab Alkaline Province (Winter and Rikhotso, 1998). Supporting this are Sm/Yb vs La/Yb ratios, suggesting a carbonated garnet peridotite source with around 6-7 % partial melting (Fig. 10D; Yu *et al.*, 2015). Negative εHf(t) values measured in the central part of the Kuboos-Bremen Line of intrusives (0 to –5; Grootpenseiland-Marinkas Quelle, Kanabeam, Bremen Complexes) are believed to result from partial melting of a metasomatised lithospheric mantle (Zech *et al.*, 2025). This would likely be similar to the Garub valley diatremes, but to confirm a mantle source, εHf-εNd isotopic values or the presence of unaltered "fresh" mantle material, such as olivines or lherzolitic xenoliths, as reported from kimberlites, are needed (e. g. Grégoire *et al.*, 2005).

Emplacement Mechanism of the Diatremes

The rapid ascent of carbonatitic and kimberlitic melts, is believed to be driven by the violent exsolution of CO_2, causing fracturing of the wall rock and creating pathways for the melt to ascend (e. g. Walter *et al.*, 2021; Russell *et al.*, 2012). The degassing of CO_2 can be explained by two main factors: decompression with decreasing depth and the decreasing solubility of CO_2 as SiO_2 content increases (~18-32 wt.%; Russel *et al.*, 2012). The disaggregation and dissolution (assimilation) of mantle debris increase SiO_2 content in the ascending melt, coupled with a drastic decrease in CO_2 solubility, thus propelling the magma through the upper mantle (Russell *et al.*, 2012). These factors can work together, creating a self-sustaining cycle that accelerates the ascent to potentially supersonic speeds (Walter *et al.*, 2021).

The primary mantle-derived melts that formed the Garub diatremes likely ascended in a similar way but underwent some modification. Assimilation of crustal material, as implied by Ce/Pb vs Sm/Nd ratios (Fig. 11E), thus facilitated the rapid ascend of the melt. At one point, the primary carbonated silicate melt began to segregate into a carbonatitic and residual silicate fraction (liquid immiscibility; e. g. Berndt and Klemme, 2022), corresponding to the two melts inferred from the two types of pelletal lapilli present (see above). This immiscibility probably occurred under crustal conditions, after the differentiation of primitive carbonated silicate melts to alkali contents exceeding 10 wt% (Brooker and Kjarsgaard, 2011; Schmidt *et al.*, 2024). Unlike primary melts from carbonated mantle, liquid immiscibility in natural CO_2-bearing silicate melts creates carbonatitic melts with high alkali contents (8–25 wt% $Na_2O + K_2O$), accounting for the formation of fenites (Schmidt *et al.*, 2024).

The carbonatitic melt and the residual silicate melt then further ascended to shallow crustal levels until fluidisation facilitated explosive emplacement. Evidence for a phreatomagmatic emplacement (e. g. Brukkaros), such as quenched magma (glassy textures) or abundant vesicles is lacking (Kurszlaukis and Lorenz, 1997), while fluidisation is supported by the presence of pelletal lapilli. The carbonatitic melt probably suffered a more violently explosive emplacement, as these samples usually contain higher amounts and larger xenoliths of Namaqua basement material. Increased explosive power could be attributed to the rapid bleaching of basement xenoliths, causing rapid CO_2 exsolution (SiO_2 contamination). This process is summarised schematically in Figure 15.

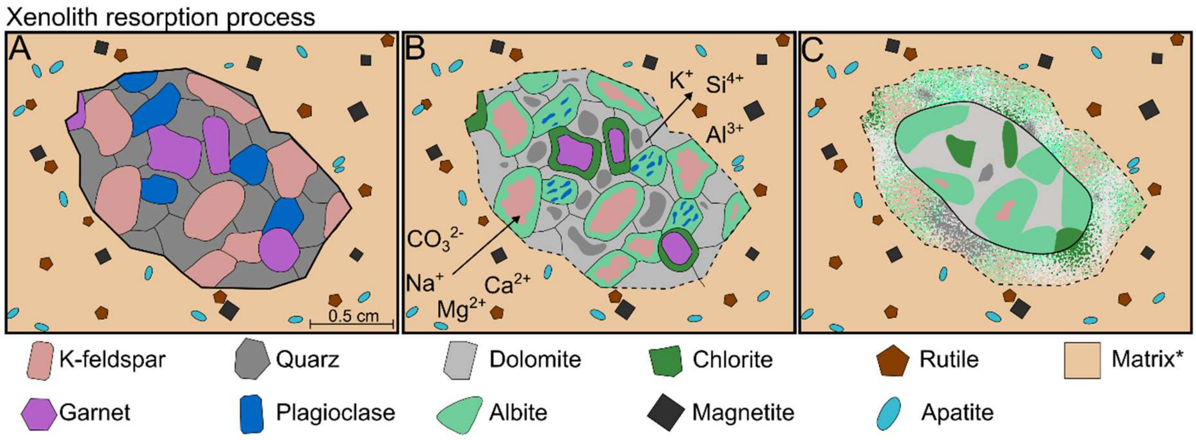

Figure 15. Schematic illustration depicting the stages of resorption of a gneissic Namaqua xenolith, composed of quartz, plagioclase, K-feldspar, and garnet (simplified composition), entrained in the diatreme-forming melt; the melt is represented by the typical observed matrix (*consisting of dolomite, albite, magnetite, rutile, and apatite). The illustration is based on elemental mappings from xenolith-rich samples (Fig. 7). A) Unaffected angular xenolith; B) Progressive albitisation, initially affecting plagioclase, followed by K-feldspar; garnet undergoes chloritisation, while quartz is replaced by dolomite. Elemental transfer between the melt and xenolith is indicated; C) Further resorption results in the shrinking of the now rounded xenolith. The halo comprises a very fine-grained mixture of K-feldspar, albite, quartz, dolomite, and chlorite.

Metasomatic Processes

Textures, mineral assemblages, and stable isotopes suggest the presence of a hydrothermal phase or overprint, which has caused alterations in the diatremes. These effects will be unravelled in the following discussion.

Xenolith Resorption

The common granitic to gneissic, frequently bleached Namaqua xenoliths, which are found in the diatreme samples, exhibit various degrees of alteration (Figs 4H & 7B, E & H), which can be so extensive that the xenoliths come to resemble the mineral composition of the matrix, including dolomite and albite. Such alteration and progressive resorption of xenoliths are commonly observed features, particularly in carbonatites (e. g. Giebel *et al.*, 2019; Walter *et al.*, 2022). Accordingly, the alteration and subsequent resorption of xenoliths are believed to result from three likely simultaneous processes, as illustrated in the paragenetic sequence (Fig. 6; numbered arrows corresponding to the processes): 1) albitisation, 2) chloritisation, and 3) dolomitisation.

Albitisation appears to be quite extensive, observable in both the host rocks and the diatreme samples. During albitisation of non-diatreme components, first plagioclase, then K-feldspar is replaced by albite. This order of replacement has been observed elsewhere (e. g. Kaur *et al.*, 2012) and is indicated by the presence of plagioclase in the country rock but not within the diatreme, with K-feldspar present in both. The presence of albite in the diatreme matrix is more difficult to explain, as it has a similar paragenetic character to dolomite, implying simultaneous crystallisation (e. g. Fig. 9E). Albite has been reported to be a major constituent (up to 65 vol. %) in the carbonatite breccia from Swartbooisdrif, and there is believed to be of hydrothermal origin pre-dating or synchronous to the carbonatite emplacement (Drüppel *et al.*, 2005).

The presence of chlorite group minerals (Figs 5E & 9B) in approximately half of the diatreme samples suggests a hydrous regime for their formation, as chloritisation is a typical reaction process in hydrothermal environments (e. g. Parneix *et al.*, 1985). There are two groups of chlorites: type 1 - trioctahedral, probably an alteration product of ultramafic minerals (Shirozu, 1978), and type 2 - dioctahedral, which could represent a primary (synmagmatic?) hydrothermal constituent. For type 2 chlorite, Al could be provided by the alteration of plagioclase to albite, while Fe and Mg are present in common garnets (almandine-pyrope) from the country rock. These elements are also available from the melt. Type 1 chlorite is likely a result of post-eruptive alteration due to intruding groundwater along the diatremes.

The observed transformation of quartz into dolomite within resorbed xenoliths is probably a magmatic process, as quartz within the surrounding wall rock is only partially affected by alteration. Since carbonatitic melts have very low viscosities (Dobson *et al*., 1996), they can behave similar to a fluid and can also act as a metasomatic agents (Vasyukova and Williams-Jones, 2022). However, this is strictly a magmatic replacement and not metasomatism.

Xenolith resorption is envisioned to transform a fresh, angular gneissic fragment into a smaller, rounded (resorbed) xenolith with a fine-grained halo of tiny minerals from the original xenolith and the melt (Figs 15A-C). Elemental transfer is believed to cause an enrichment in Na, Mg, Ca, and CO_3 and a release of K, Si, and Al. This is supported by increased modal albite within the xenolith compared to pre-alteration modal plagioclase and K-feldspar.

Fenitisation

Fenitisation is partially observed at the Garub diatremes, as noted by Schreuder (1975). In the studied samples it can be categorised into two groups based on host rock type. Within the gneissic Namaqua host rock it is more pronounced due to its coarser texture and mineral composition, which is more susceptible to fenitisation (e. g. feldspar, quartz). In the Nama host rock fenitisation is observed in samples with direct contact relationships (GRB026F) to the diatreme. Evidence for fenitisation include the high abundance of albite/oligoclase in the Namaqua basement, along with turbid K-feldspars exhibiting perthite textures. Small biotite grains may also be of metasomatic origin. Fenitisation of the Schwarzrand sediments is less prominent. Where the diatreme is in direct contact with the Nama host rock, SEM analysis reveals abundant albite, as well as minor aegirine and magnesio-arfvedsonite, typical of sodic fenites (Fig. 9G; Elliott *et al*., 2018). The lack of evidence for potassic fenitisation at the Garub diatremes does not necessarily imply it did not occur.

Spatial and temporal variations in fenites are influenced by temperature, pressure, and CO^2 content of the fenitising fluid (Rubie and Gunter, 1983). K is more mobile at lower temperatures, forming shallower potassic fenites, while sodium is lost from fluids at deeper levels (>600°C), creating deeper sodic fenites (Elliot *et al*., 2018). The presence of K-feldspar rimmed by albite (Ruri Hills, Kenya and Koga, Pakistan), along with K-feldspar-rich fenite cut by albite veins (Bayan Obo, China; Le Bas, 2008), shows that sodic fenitisation can also follow potassic fenitisation.

The high abundance of K-feldspar in the Namaqua basement gneiss, would balance any potential chemical gradient, making a potassic fenitisation less prominent, while the low Na content in the basement gneiss creates a high gradient, allowing for more intense sodic fenitisation. However, it is believed that a major potassic fenitising fluid was not involved; rather, a highly sodic fluid led to the release of K, as indicated by the moderate albitisation of K-feldspar in the basement. The released K is probably available to form the non-macrocrystal phlogopite present in the matrix of some samples (Figs 7C, E & H).

The hydrothermal overprint, evidenced by the abundant albite within the diatremes and the wall rock, is most likely due to the same fluid expelled from the carbonatitic melt during its ascent and emplacement. The presence of abundant gneissic xenoliths and the high levels of Si and Al contamination made the carbonatitic, tuffisitic rock equally susceptible to metasomatism. Since multiple pulses of sodic aqueous fluids are typical (Elliot *et al*., 2018), these fluids would be capable of fenitising both the wall rock and diatreme rocks, predominantly through albitisation. To gain a better understanding of these fluids, further studies are necessary.

Age and Geological Setting

The age of 491 ± 8 Ma, derived from Rb-Sr analyses on whole rock and biotite, can be considered as a lower limit (Allsopp *et al*., 1979). Recent biotite Ar-Ar dating yields ages of 523 and 527 (±2) Ma (Zech *et al*., 2025), corroborating earlier Ar-Ar ages ranging from 514 to 524 Ma (Spriggs, 1988). These Ar-Ar ages were determined from KAP rocks approximately 30 km south of the Garub valley and may not necessarily reflect the exact age of the intrusives within the Garub valley itself. For instance, the Hegau-Urach (Germany) volcanic region hosts numerous ultramafic volcanics across a comparable area, exhibiting age spans of 19–12 Ma (Urach) and 15–9 Ma (Hegau) of continuous volcanic activity (Binder *et al*., 2023). Therefore, it is likely that the KAP encompasses ages spanning several million years, similar to the KBL, which does not show any age progression tracks, but rather an age range of approximately 70 million years (Zech *et al*., 2025 and references therein).

The Great Karas Mountains, in which the Garub valley is located, are characterised by an extensive sedimentary cover of Fish River Subgroup (Fig. 1B), apparently barren of KAP intrusions. This implies that the Garub valley diatremes erupted through the Schwarzrand Subgroup (dated from 545.27 ± 0.11 Ma to 538.58 ± 0.19 Ma; Nelson *et al*., 2022; Linnemann *et al*., 2019), forming sills and pipes, but did not penetrate the Fish River Subgroup, which in turn argues for emplacement prior to the deposition of the Fish River Subgroup.

The most plausible stratigraphic age is associated with the Nomtsas Formation, specifically the ash bed W8 (538.58 ± 0.19 Ma; Linnemann *et al*., 2019), which unconformably overlies the Urusis Formation (Fig. 2).

Within a similar time frame, the Pan-African orogenies led to the formation of the Damara, Kaoko and Gariep Belts (e. g. Miller, 1983; Gray *et al*., 2006; Frimmel, 2008). The latter extends along the coast of southern Namibia (Fig. 1A), approximately 200 km west of the Garub valley. It has a collision-related metamorphic age of around 550-540 Ma (Frimmel and Frank, 1998). The Nama Group, interpreted as foreland basin sediments resulting from orogenic crustal thickening and subsequent erosion (Germs, 1983), indicates that the KAP intrusives were emplaced within the farther field of influence of this orogeny. This aligns with the fact that 75% of all carbonatites have erupted within 600 km of craton edges or within 2200 km of orogenic events (Humphreys-Williams and Zahirovic, 2021), both of which applies to the KAP intrusives.

Trigger for Emplacement

The intrusive complexes along the Kuboos–Bremen Line do not align with existing regional Namaquan or Gariepian geological structures. Instead, they cross-cut established boundaries leaving their tectonic emplacement mechanism poorly understood (Zech *et al*., 2025). Their formation likely resulted from far-field effects associated with the contemporaneous Pan-African orogenies, which may also apply locally within the KAP. A plausible scenario is that asthenospheric upwelling along the KBL caused the magmatism, possibly related to the syn-convergent extension during intracontinental orogeny as, for instance, proposed for the Heping pluton in China (Xie *et al.,* 2020).

A major NNE-trending reverse fault system traversing the Great Karas Mountains (Karasburg graben shoulder) lies immediately to the west of the Garub valley (Fig. 1A), while approximately 20 km northeast of the valley, the NE-trending Trans-Kalahari Lineament, a deep-seated, crustal-scale fault, intersects the SE-trending Lord Hill-Excelsior shear zone, which forms the northern boundary of the Namaquan Kakamas Domain (Corner, 2000; Macey *et al*., 2022). Although diatremes of the Kainab Alkaline Province were rarely emplaced along these major structures (Fig. 1), satellite imagery reveals smaller fault systems and dykes within the Garub valley (Fig. 2).

Examination of magnetic imagery from the Grünau area reveals that the western KAP intrusions are frequently located on NNE-trending magnetic lineaments that represent dolerite dykes of the Gannakouriep swarm. Geophysical data for the eastern KAP has not been studied. During regional mapping by the Geological Survey of Namibia and Council for Geoscience (South Africa) faults were observed that formed along and reworked the Gannakouriep dykes (e. g. Macey *et al*., 2020). The mapping also revealed that faults were active during Nama Group deposition, with blind faults that displaced lower Nama Group units overlain by younger, unaffected Nama sediments. Ar-Ar dating of the NNE-striking Oup fault SE of the Garub valley revealed an age of about 512 Ma (Büttner *et al*., 2013), confirming faulting was active during Nama times. Given that Garub bodies intruded during the deposition of the Nama Group, and apparently along reworked Tonian dykes, we hypothesise that pre-existing deep Gannakouriep structures, reactivated during the development of the Nama Basin, provided the pathways for the emplacement of the diatreme-forming melts (Fig. 14).

Conclusions

The classification of the KAP rocks is complicated by their tuffisitic nature and contamination, which obscure the original melt composition. The examined rocks exhibit traits of both ultramafic and carbonatitic types in terms of emplacement style, texture, mineralogy, and alteration effects. While they are best described as carbonatitic, strict classification remains to be solved, with a focus on understanding their formative processes rather than rigid nomenclature.

Mineralogically, the Garub valley rocks include dolomite, albite, phlogopite, quartz, magnetite, rutile, apatite, clinochlore, calcite, and baryte, indicating both magmatic and hydrothermal origins. Stable isotope data confirm significant hydrothermal influence. Two distinct melt types are inferred: a diopside-bearing ultramafic melt and a silicate-free carbonatitic melt, likely derived from the first. Syn-magmatic hydrothermal fluids caused extensive albitisation and fenitisation, with diagnostic minerals like aegirine and arfvedsonite. Additional hydrothermal phases suggest carbonatitic influence but lack ore elements.

Country-rock xenolith resorption involved both magmatic and hydrothermal processes, introducing elements like Na, Mg, Ca, and C into xenoliths while releasing Si, Al, and K into the melt, contributing to contamination. Despite variations among diatremes, geochemical data indicate a common mantle source, with melt generated probably from carbonated garnet peridotite. Phlogopite, diopside, and ilmenite phenocrysts suggest a metasomatised subcontinental lithospheric mantle source.

An emplacement age of approximately 540 Ma is proposed, possibly along pre-existing Tonian Gannakouriep dykes, reactivated during the development of the Nama Basin in the foreland of the evolving Gariep and Damara Orogens.

Acknowledgements

The authors would like to thank Axel Müller for reviewing this article and providing insightful comments. Appreciation is also extended to Ute Schreiber for editorial guidance. Thanks are given to Cordelia Lange for her assistance in facilitating the measurement of sample compositions, as well as to Elisabeth Eiche, Tobias Kluge, Maya Denker, and Claudia Mössner for conducting the whole rock and isotope analyses. The authors would also like to thank Jorge Arthuzzi for joining the fieldwork and providing valuable field observations and insights. This study was supported by DFG (Deutsche Forschungsgemeinschaft) grants WA3116/14-1, GI1499/5-1, and MA 2563-25.

References

Al-Aasm, I. S., Taylor, B. E. and South, B. 1990. Stable isotope analysis of multiple carbonate samples using selective acid extraction. *Chemical Geology: Isotope Geoscience section,* **80**, 119–125.

Allsopp, H. L., Kostlin, E. O., Welke, H. J., Burger, A. J., Kröner, A. and Blignault, H. J. 1979. Rb-Sr and U-Pb geochronology of late Precambrian-early Palaeozoic igneous activity in the Richtersveld (South Africa) and southern South West Africa. *Transactions of the Geological Society of South Africa*, **82**, 185–204.

Anenburg, M., Broom-Fendley, S. and Chen, W. 2021. Formation of Rare Earth Deposits in Carbonatites. *Elements*, **17**, 327–332.

Baudrand, M., Aloisi, G., Lécuyer, C., Martineau, F., Fourel, F., Escarguel, G., Blanc-Valleron, M.-M., Rouchy, J.-M. and Grossi, V. 2012. Semi-automatic determination of the carbon and oxygen stable isotope compositions of calcite and dolomite in natural mixtures. *Applied Geochemistry,* **27**, 257–265.

Bell, K. and Tilton, G. R. 2001. Nd, Pb and Sr Isotopic Compositions of East African Carbonatites: Evidence for Mantle Mixing and Plume Inhomogeneity. *Journal of Petrology*, **42**, 1927–1945.

Berndt, J. and Klemme, S. 2022. Origin of carbonatites—liquid immiscibility caught in the act. *Nature Communications*, **13**, https://doi.org/10.1038/s41467-022-30500-7

Bial, J., Büttner, S. and Appel, P. 2016. Timing and conditions of regional metamorphism and crustal shearing in the granulite facies basement of south Namibia: Implications for the crustal evolution of the Namaqualand metamorphic basement in the Mesoproterozoic. *Journal of African Earth Sciences*, **123**, 145–176.

Binder, T., Marks, M. A. W., Gerdes, A., Walter, B. F., Grimmer, J., Beranoaguirre, A., Wenzel, T. and Markl, G. 2023. Two distinct age groups of melilitites, foidites, and basanites from the southern Central European Volcanic Province reflect lithospheric heterogeneity. *International Journal of Earth Sciences*, **112**, 881–905.

Brooker, R. A. and Kjarsgaard, B. A. 2011. Silicate–Carbonate Liquid Immiscibility and Phase Relations in the System SiO_2 – Na_2O - Al_2O_3 – CaO - CO_2 at 0.1 – 2.5 GPa with Applications to Carbonatite Genesis. *Journal of Petrology*, **52**, 1281–1305.

Büttner, S. H., Sherlock, S., Fryer, L., Lodge, J., Diale, T., Kazondunge, R. and Macey, P. 2013. Controls of host rock mineralogy and H_2O content on the nature of pseudotachylyte melts: Evidence from Pan-African faulting in the foreland of the Gariep Belt, South Africa. *Tectonophysics*, **608**, 552–575.

Carnevale, G. and Zanon, V. 2024. Characterisation of Pelletal Lapilli in Explosive Melilitite–Carbonatite Eruptions: An Example from Mt. Vulture Volcano (Southern Italy). *Geosciences*, **14(12)**, https://doi.org/10.3390/geosciences14120349

Clement, C. 1982. *A comparative geological study of some major kimberlite pipes in the Northern Cape and Orange Free State*. Ph.D. thesis, University of Cape Town, South Africa, 451 pp.

Clement, C. R. and Skinner, E. M. W. 1985. A textural-genetic classification of kimberlites. *South African Journal of Geology*, **88**, 403–409.

Corner, B. 2000. Crustal framework of Namibia derived from magnetic and gravity data. *Communications of the Geological Survey of Namibia*, **12**, 15–22.

Dasgupta, R., Hirschmann, M. M., McDonough, W. F., Spiegelman, M. and Withers, A. C. 2009. Trace element partitioning between garnet lherzolite and carbonatite at 6.6 and 8.6 GPa with applications to the geochemistry of the mantle and of mantle-derived melts. *Chemical Geology*, **262**, 57–77.

Dasgupta, R., Mallik, A., Tsuno, K., Withers, A. C., Hirth, G. and Hirschmann, M. M. 2013. Carbon dioxide-rich silicate melt in the Earth's upper mantle. *Nature*, **493**, 211–215.

Davies, D. R. and Rawlinson, N. 2014. On the origin of recent intraplate volcanism in Australia. *Geology*, **42**, 1031–1034.

Deines, P. 1989. Stable isotope variations in carbonatites, 301–359. *In*: In Bell, K. (Ed.) *Carbonatites: Genesis and Evolution*. Unwin Hyman, London, UK, 618 pp.

DIGIS Team 2025. *GEOROC Compilation: Rock Types*. Georg-August Universität Göttingen, Germany, https://doi.org/10.25625/2JETOA

Dobson, D. P., Jones, A. P., Rabe, R., Sekine, T., Kurita, K., Taniguchi, T., Kondo, T., Kato, T., Shimomura, O. and Satoru Urakawa, S. 1996. In-situ measurement of viscosity and density of carbonate melts at high pressure. *Earth and Planetary Science Letters*, **143**, 207–215.

Dongre, A. and Tappe, S. 2019. Kimberlite and carbonatite dykes within the Premier diatreme root (Cullinan Diamond Mine, South Africa): New insights to mineralogical-genetic classifications and magma CO_2 degassing. *Lithos*, **338–339**, 155–173.

Doroshkevich, A. G., Chebotarev, D. A., Sharygin, V. V., Prokopyev, I. R. and Nikolenko, A. M. 2019. Petrology of alkaline silicate rocks and carbonatites of the Chuktukon massif, Chadobets upland, Russia: Sources, evolution and relation to the Triassic Siberian LIP. *Lithos*, **332–333**, 245–260.

Downes, H., Balaganskaya, E., Beard, A., Liferovich, R. and Demaiffe, D. 2005. Petrogenetic processes in the ultramafic, alkaline and carbonatitic magmatism in the Kola Alkaline Province: A review. *Lithos*, **85**, 48–75.

Drüppel, K., Hoefs, J. and Okrusch, M. 2005.

Fenitizing Processes Induced by Ferrocarbonatite Magmatism at Swartbooisdrif, NW Namibia. *Journal of Petrology*, **46**, 377–406.

Elliott, H. A. L., Wall, F., Chakhmouradian, A. R., Siegfried, P. R., Dahlgren, S., Weatherley, S., Finch, A. A., Marks, M. A. W., Dowman, E. and Deady, E. 2018. Fenites associated with carbonatite complexes: A review. *Ore Geology Reviews*, **93**, 38–59.

Foley, S. F., Yaxley, G. M. and Kjarsgaard, B. A. 2019. Kimberlites from source to surface: insights from experiments. *Elements*, **15**, 393–398.

Frimmel, H. E. 2008. The Gariep Belt. *In*: Miller, R. McG. (Ed.). *The Geology of Namibia*, Vol. **2**, chapter 14, 40 pp. Geological Society of Namibia, Windhoek.

Frimmel, H. E. and Frank, W. 1998. Neoproterozoic tectono-thermal evolution of the Gariep Belt and its basement, Namibia and South Africa. *Precambrian Research*, **90**, 1–28.

Frimmel, H. E., Zartman, R. E. and Späth, A. 2001. The Richtersveld Igneous Complex, South Africa: U-Pb Zircon and Geochemical Evidence for the Beginning of Neoproterozoic Continental Breakup. *The Journal of Geology*, **109**, 493–508.

Germs, G. J. B. 1983. Implications of a sedimentary facies and depositional environmental analysis of the Nama Group in South West Africa/Namibia, 89–114. *In*: Miller, R. McG. (Ed.), Evolution of the Damara Orogen of South West Africa/ Namibia. *Special Publications of the Geological Society of South Africa*, **11**, 515 pp.

Gernon, T. M., Brown, R. J., Tait, M. A. and Hincks, T. K. 2012. The origin of pelletal lapilli in explosive kimberlite eruptions. *Nature Communications*, **3**, https://doi.org/10.1038/ncomms1842

Geyer, G. 2005. The Fish River Subgroup in Namibia: stratigraphy, depositional environments and the Proterozoic–Cambrian boundary problem revisited. *Geological Magazine*, **142**, 465–498.

Giebel, R. J., Parsapoor, A., Walter, B. F., Braunger, S., Marks, M. A. W., Wenzel, T. and Markl, G. 2019. Evidence for Magma–Wall Rock Interaction in Carbonatites from the Kaiserstuhl Volcanic Complex (Southwest Germany). *Journal of Petrology*, **60**, 1163–1194.

Gittins, J. and Harmer, R. E. 1997. What is ferrocarbonatite? A revised classification. *Journal of African Earth Sciences*, **25**, 159–168.

Giuliani, A., Phillips, D., Kamenetsky, V. S., Fiorentini, M. L., Farquhar, J. and Kendrick, M. A. 2014. Stable isotope (C, O, S) compositions of volatile-rich minerals in kimberlites: A review. *Chemical Geology*, **374–375**, 61–83.

Giuliani, A., Pearson, D. G., Soltys, A., Dalton, H., Phillips, D., Foley, S. F., Lim, E., Goemann, K., Griffin, W. L. and Mitchell. R. H. 2020. Kimberlite genesis from a common carbonate-rich primary melt modified by lithospheric mantle assimilation. *Science Advances*. **6(17)**, https://doi.org/10.1126/ sciadv.aaz0424

Giuliani, A., Dalton, H. and Pearson, D. G. 2025. Kimberlites: The deepest geochemical probes of Earth, 159–230. *In*: Anbar, A. and Weis, D. (Eds) *Treatise on Geochemistry*, Elsevier, Amsterdam, Netherlands.

Gray, D. R., Foster, D. A., Goscombe, B., Passchier, C. W. and Trouw, R. A. J. 2006. $^{40}Ar/^{39}Ar$ thermochronology of the Pan-African Damara Orogen, Namibia, with implications for tectonothermal and geodynamic evolution. *Precambrian Research*, **150**, 49–72.

Grégoire, M., Tinguely, C., Bell, D. R. and Le Roex, A. P. 2005. Spinel lherzolite xenoliths from the Premier kimberlite (Kaapvaal craton, South Africa): Nature and evolution of the shallow upper mantle beneath the Bushveld complex. *Lithos*, **84**, 185–205.

Haggerty, S. E. 1994. Superkimberlites: A geodynamic diamond window to the Earth's core. *Earth and Planetary Science Letters*, **122**, 57–69.

Harris, C., Le Roux, P., Cochrane, R., Martin, L., Duncan, A. R., Marsh, J. S., Le Roex, A. P. and Class, C. 2015. The oxygen isotope composition of Karoo and Etendeka picrites: High $\delta^{18}O$ mantle or crustal contamination? *Contributions to Mineralogy and Petrology*, **170**, 8.

Hofmann, A. W., Jochum, K. P., Seufert, M. and White, W. M. 1986. Nb and Pb in oceanic basalts: new constraints on mantle evolution. *Earth and Planetary Science Letters*, **79**, 33–45.

Horstmann, U. E. and Verwoerd, W. J. 1997. Carbon and oxygen isotope variations in southern African carbonatites. *Journal of African Earth Sciences*, **25**, 115–136.

Humphreys-Williams, E. R. and Zahirovic, S. 2021. Carbonatites and Global Tectonics. *Elements*, **17**, 339–344.

Kamenetsky, V. S. 2016. Comment on: “The ascent of kimberlite: Insights from olivine” by Brett *et al*., 2015 [*Earth Planet. Sci. Lett*., **424**, 119–131]. *Earth and Planetary Science Letters*, **440**, 187–189.

Kamenetsky, V. S., Doroshkevich, A. G., Elliott, H. A. L. and Zaitsev, A. N. 2021. Carbonatites: Contrasting, Complex, and Controversial. *Elements*, **17**, 307–314.

Kapustin, Y. L. 1981. Damkjernites—dike equivalents of carbonatites. *International Geology Review*, **23**, 1326–1334.

Kaur, P., Chaudhri, N., Hofmann, A. W., Raczek, I., Okrusch, M., Skora, S. and Baumgartner, L. P. 2012. Two-Stage, Extreme Albitization of A-type Granites from Rajasthan, NW India. *Journal of Petrology*, **53**, 919–948.

Keller, J. and Hoefs, J. 1995. Stable Isotope Characteristics of Recent Natrocarbonatites from Oldoinyo Lengai, 113-123. *In*: Bell, K. and Keller, J. (Eds) *Carbonatite Volcanism: Oldoinyo Lengai and the Petrogenesis of Natrocarbonatites*. Springer, 210 pp.

Kim, S.-T., Coplen, T. B. and Horita, J. 2015. Normalization of stable isotope data for carbonate minerals: Implementation of IUPAC guidelines. *Geochimica et Cosmochimica Acta*, **158**, 276–289.

Kjarsgaard, B. A., Pearson, D. G., Tappe, S., Nowell, G. M. and Dowall, D. P. 2009. Geochemistry of hypabyssal kimberlites from Lac de Gras, Canada: Comparisons to a global database and applications to the parent magma problem. *Lithos*, **112**, 236–248.

Krmíček, L. and Chalapathi Rao, N. V. 2022. Lamprophyres, lamproites and related rocks as tracers to supercontinent cycles and metallogenesis. *In*: Krmíček, L. and Chalapathi Rao, N. V. (Eds), Lamprophyres, Lamproites and Related Rocks: Tracers to Supercontinent Cycles and Metallogenesis. *Geological Society, London, Special Publications*, **513**, 1-16.

Kurszlaukis, S. and Lorenz, V. 1997. Volcanological features of a low-viscosity melt: the carbonatitic Gross Brukkaros Volcanic Field, Namibia. *Bulletin of Volcanology*, **58**, 421–431.

Le Bas, M. J. 2008. Fenites associated with carbonatites. *The Canadian Mineralogist*, **46**, 915–932.

Le Maitre, R. W., Streckeisen, A., Zanettin, B., Le Bas, M. J., Bonin, B. and Bateman, P. (Eds) 2002. *Igneous Rocks: A Classification and Glossary of Terms*. Cambridge University Press, Cambridge, UK, 236 pp.

Linnemann, U., Ovtcharova, M., Schaltegger, U., Gärtner, A., Hautmann, M., Geyer, G., Vickers-Rich, P., Rich, T., Plessen, B., Hofmann, M., Zieger, J., Krause, R., Kriesfeld, L. and Smith, J. 2019. New high-resolution age data from the Ediacaran–Cambrian boundary indicate rapid, ecologically driven onset of the Cambrian explosion. *Terra Nova*, **31**, 49–58.

Lloyd, F. and Stoppa, F. 2003. Pelletal Lapilli in Diatremes - Some Inspiration from the Old Masters. *GeoLines*, **15**, 65-71.

Macey, P. H., Minnaar, H., Miller, J. A., Lambert, C. W., Kisters, A. F., Diener, J. F. A, Thomas, R. J., Groenewald, C. A. Indongo, J., Angombe, M., Smith, H., Shifotoka, G., Le Roux. P., and Frei, D. 2020. The Precambrian Geology of the Warmbad region, Southern Namibia, Chapter 8 – Post-Namaqua intrusions and superficial deposits. Unpublished Report Council for Geoscience (South Africa)/Geological Survey of Namibia, 72 pp.

Macey, P. H., Thomas, R. J., Kisters, A. F. M., Diener, J. F. A, Angombe, M., Doggart, S., Groenewald, C. A., Lambert, C. W., Miller, J. A., Minnaar, H., Smith, H., Moen, H. F. G., Muvangua, E., Nguno, A., Shifotoka, G., Indongo, J., Frei, D., Spencer, C., Le Roux. P., Armstrong, R. A. and Tinguely, C. 2022. A continental back-arc setting for the Namaqua belt: Evidence from the Kakamas Domain. *Geoscience Frontiers*, **13,** https://doi.org/10.1016/j.gsf.2022.101408

Massuyeau, M., Gardés, E., Morizet, Y. and Gaillard, F. 2015. A model for the activity of silica along the carbonatite–kimberlite–mellilitite–basanite melt compositional joint. *Chemical Geology*, **418**, 206–216.

Mattsson, H. B., Högdahl, K., Carlsson, M. and Malehmir, A. 2019. The role of mafic dykes in the petrogenesis of the Archean Siilinjärvi carbonatite complex, east-central Finland. *Lithos*, **342–343**, 468–479.

Miller, R. McG. 1983. The Pan-African Damara Orogen of South West Africa/Namibia, 431-515. *In*: Miller, R. McG. (Ed.), Evolution of the Damara Orogen of South West Africa/ Namibia. *Special Publications of the Geological Society of South Africa*, **11**, 515 pp.

Miller, R. McG. 2012. Review of Mesoproterozoic magmatism, sedimentation and terrane amalgamation in southwestern Africa. *South African Journal of Geology*, **115**, 417–448.

Mitchell, R. H. 1986. *Kimberlites. Mineralogy, Geochemistry, and Petrology*. Plenum Press, New York, London, 442 pp.

Mitchell, R. H. 1995. Kimberlites and Orangeites. 1–90. *In*: Mitchell, R. H. (Ed.) *Kimberlites, Orangeites, and Related Rocks*. Springer, New York (USA), 424 pp.

Mitchell, R. H. 2005. Carbonatites and carbonatites and carbonatites. *The Canadian Mineralogist*, **43**, 2049–2068.

Mitchell, R. H., Giuliani, A. and O'Brien, H. 2019. What is a Kimberlite? Petrology and Mineralogy of Hypabyssal Kimberlites. *Elements*, **15**, 381–386.

Moore, K. R., Brady, A. E. and Costanzo, A. 2022. Crystal-Liquid Segregation in Silicocarbonatite Magma Leads to the Formation of Calcite Carbonatite. *Journal of Petrology*, **63**, https://doi.org/10.1093/petrology/egac056

Muir, R. A., Whitehead B. A., New T., Stevens V., Macey P. H., Groenewald C. A., Salomon G., Kahle B., Hollingsworth J., Sloan R. A. 2023. Exceptional Scarp Preservation in SW Namibia Reveals Geological Controls on Large Magnitude Intraplate Seismicity in Southern Africa. *Tectonics* **42**, https://doi.org/10.1029/2022TC007693

Munro, J. and Harris, C. 2023. A High-δ^{18}O Mantle Source for the 2.06 Ga Phalaborwa Igneous Complex, South Africa? *Journal of Petrology*, **64**, https://doi.org/10.1093/petrology/egad063

Nasir, S., Al-Khirbash, S., Rollinson, H., Al-Harthy, A., Al-Sayigh, A., Al-Lazki, A., Theye, T., Massonne, H.-J. and Belousova, E. 2011. Petrogenesis of early cretaceous carbonatite and ultramafic lamprophyres in a diatreme in the Batain Nappes, Eastern Oman continental margin. *Contributions to Mineralogy and Petrology*, **161**, 47–74.

Nelson, L. L., Ramezani, J., Almond, J. E., Darroch, S. A. F., Taylor, W. L., Brenner, D. C., Furey, R. P., Turner, M. and Smith, E. F. 2022. Pushing the boundary: A calibrated Ediacaran-Cambrian stratigraphic record from the Nama Group in northwestern Republic of South Africa. *Earth and Planetary Science Letters*, **580**, https://doi.org/10.1016/ j.epsl.2022.117396

Nordin, F. 2009. *U-Pb dating, Lu-Hf isotopic analyses and geothermobarometry of rocks in the Grünau Terrane and Richtersveld Subprovince, Namaqua Sector, southern Africa*. M. Sc. thesis, University Gothenburg, Sweden, 52 pp.

Obata, M. 2011. Kelyphite and symplectite: textural and mineralogical diversities and universality, and a new dynamic view of their structural formation. *In*: Sharkow, E. (Ed.) *New Frontiers in Tectonic Research - General Problems, Sedimentary Basins and Island Arcs*. InTech, DOI: 10.5772/20265

Parneix, J. C., Beaufort, D., Dudoignon, P. and Meunier, A. 1985. Biotite chloritization process in hydrothermally altered granites. *Chemical Geology*, **51**, 89–101.

Pilbeam, L. H., Nielsen, T. F. D., Waight, T. and Tappe, S. 2024. Links between Calcite Kimberlite, Aillikite and Carbonatite in West Greenland: Numeric Modeling of Compositional Relationships. *Journal of Petrology*, **65**, https://doi.org/10.1093/petrology/egae059

Prokopyev, I. R., Borisenko, A. S., Borovikov, A. A. and Pavlova, G. G. 2016. Origin of REE-rich ferrocarbonatites in southern Siberia (Russia): implications based on melt and fluid inclusions. *Mineralogy and Petrology*, **110**, 845–859.

Prokopyev, I., Starikova, A., Doroshkevich, A., Nugumanova, Y. and Potapov, V. 2020. Petrogenesis of Ultramafic Lamprophyres from the Terina Complex (Chadobets Upland, Russia): Mineralogy and Melt Inclusion Composition. *Minerals*, **10**, https://doi.org/10.3390/min10050419

Prokopyev, I., Doroshkevich, A., Starikova, A., Kovalev, S., Nugumanova, Y. and Izokh, A. 2023. Petrogenesis of juvenile pelletal lapilli in ultramafic lamprophyres. *Scientific Reports*, **13**, https://doi.org/10.1038/s41598-023-32535-2

Reid, D. L. 1991. Alkaline rocks in the Kuboos-Bremen igneous province, southern Namibia: the Kanabeam multiple ring complex. *Communications of the Geological Survey of Namibia*, **7**, 3–13.

Reid, D. L. and Cooper, A. F. 1992. Oxygen and carbon isotope patterns in the Dicker Willem carbonatite complex, southern Namibia. *Chemical Geology*, **94**, 293–305.

Ries, J. B., Fike, D. A., Pratt, L. M., Lyons, T. W. and Grotzinger, J. P. 2009. Superheavy pyrite (δ^{34}Spyr > δ^{34}SCAS) in the terminal Proterozoic Nama Group, southern Namibia: A consequence of low seawater sulfate at the dawn of animal life. *Geology*, **37(8)**, 743-746.

Rioux, M., Bowring, S., Dudás, F. and Hanson, R. 2010. Characterizing the U–Pb systematics of baddeleyite through chemical abrasion: application of multi-step digestion methods to baddeleyite geochronology. *Contributions to Mineralogy and Petrology*, **160**, 777–801.

Rock, N. M. S. 1986. The Nature and Origin of Ultramafic Lamprophyres: Alnöites and Allied Rocks. *Journal of Petrology*, **27**, 155–196.

Rubie, D. C. and Gunter, W. D. 1983. The role of speciation in alkaline igneous fluids during fenite metasomatism. *Contributions to Mineralogy and Petrology*, **82**, 165–175.

Rudnick, R. L. and Gao, S. 2003. Composition of the Continental Crust. *In*: Holland, H. D. and Turekian, K. K. (Eds) *Treatise on Geochemistry,* **3,** Pergamon, Oxford (UK), 64 pp.

Russell, J. K., Porritt, L. A., Lavallée, Y. and Dingwell, D. B. 2012. Kimberlite ascent by assimilation-fuelled buoyancy. *Nature*, **481**, 352–356.

Russell, J. K., Sparks, R. S. J. and Kavanagh, J. L. 2019. Kimberlite Volcanology: Transport, Ascent, and Eruption. *Elements*, **15**, 405–410.

Saylor, B. Z., Poling, J. M. and Huff, W. D. 2005. Stratigraphic and chemical correlation of volcanic ash beds in the terminal Proterozoic Nama Group, Namibia. *Geological Magazine*, **142**, 519–538.

Schmidt, M. W., Giuliani, A. and Poli, S. 2024. The origin of carbonatites—combining the rock record with available experimental constraints. *Journal of Petrology*, **65(10)**, https://doi.org/10.1093/petrology/egae105

Schreuder, C. P. 1975. *Carbonate-bearing eruptives between the Great Karas Mountains and the Bremen igneous complex, South West Africa*. M.Sc. thesis, University of Stellenbosch, South Africa, 66 pp.

Scott Smith, B. H., Nowicki, T. E., Russell, J. K., Webb, K. J., Mitchell, R. H., Hetman, C. M. and Robey, J. v. A. 2018. *A Glossary of Kimberlite and Related Terms*. Scott-Smith Petrology Inc., North Vancouver, Canada, Part 1–144 pp, Part2–59 pp, Part 3–56 pp.

Shavers, E. J., Ghulam, A., Encarnacion, J., Bridges, D. L. and Luetkemeyer, P. B. 2016. Carbonatite associated with ultramafic diatremes in the Avon Volcanic District, Missouri, USA: Field, petrographic, and geochemical constraints. *Lithos*, **248–251**, 506–516.

Shirozu, H. 1978. Chapter 7: Chlorite minerals, 243–264. *In*: Sudo, T. and Shimoda, S. (Eds) Clays and Clay Minerals of Japan, *Developments in Sedimentology*, **26**, Elsevier, Amsterdam, Netherlands.

Siedner, G. and Mitchell, J. G. 1976. Episodic mesozoic volcanism in Namibia and Brazil: A K-Ar Isochron study bearing on the opening of the South Atlantic. *Earth and Planetary Science Letters*, **30**, 292–302.

Smith, C. B., Haggerty, S. E., Chatterjee, B., Beard, A. and Townend, R. 2013. Kimberlite, lamproite, ultramafic lamprophyre, and carbonatite relationships on the Dharwar Craton, India; an example from the Khaderpet pipe, a diamondiferous ultramafic with associated carbonatite intrusion. *Lithos*, **182–183**, 102–113.

Smith, M., Kynicky, J., Chen, X., Wenlei, S., Spratt, J., Jeffries, T., Brtnicky, M., Kopriva, A. and Cangelosi, D. 2018. The origin of secondary heavy rare earth element enrichment in carbonatites: Constraints from the evolution of the Huanglongpu district, China. *Lithos*, **308-309**, 65-82.

Smithies, R. H. 1991. *The geochemical evolution of three alkaline complexes in the Kuboos-Bremen igneous province, southern Namibia. South Africa*. Ph. D. Thesis, Rhodes University, Grahamstown, South Africa, 196 pp.

Söhnge, P. G. and De Villiers, J. 1948. The Kuboos pluton and its associated line of intrusives. *Transactions of the Geological Society of South Africa*, **51**, 1–31.

Sparks, R. S. J. 2013. Kimberlite Volcanism. *Annual Review of Earth and Planetary Sciences*, **41**, 497–528.

Sparks, R. S. J., Baker, L., Brown, R. J., Field, M., Schumacher, J., Stripp, G. and Walters, A. 2006. Dynamical constraints on kimberlite volcanism. *Journal of Volcanology and Geothermal Research*, **155**, 18–48.

Spiering, B. R., Bissick, A., Darroch, S. A. F., Davies, J. H. F. L., Gibson, B. M., Halverson, G. P., Laflamme, M. and Hilgen, F. J. 2023. Initial cyclostratigraphy of the middle Nama Group (Schwarzrand Subgroup) in southern Namibia. *Precambrian Research*, **397**, https://doi.org/10.1016/j.precamres.2023.107200

Spriggs, A. J. 1988. *An isotopic and geochemical study of kimberlites and associated alkaline rocks from Namibia*. Ph.D. thesis, University of Leeds, UK, 308 pp.

Sun, S.-S. and McDonough, W. F. 1989. Chemical and isotopic systematics of oceanic basalts: implications for mantle composition and processes. *In*: Saunders, A.D. and Norry, M. J. (Eds), Magmatism in the Ocean Basins. *Geological Society, London, Special Publications*, **42**, 313–345.

Tappe, S., Foley, S. F., Jenner, G. A. and Kjarsgaard, B. A. 2005. Integrating Ultramafic Lamprophyres into the IUGS Classification of Igneous Rocks: Rationale and Implications. *Journal of Petrology*, **46**, 1893–1900.

Tappe, S., Foley, S. F., Jenner, G. A., Heaman, L. M., Kjarsgaard, B. A., Romer, R. L., Stracke, A., Joyce, N. and Hoefs, J. 2006. Genesis of Ultramafic Lamprophyres and Carbonatites at Aillik Bay, Labrador: a Consequence of Incipient Lithospheric Thinning beneath the North Atlantic Craton. *Journal of Petrology*, **47**, 1261–1315.

Tappe, S., Foley, S. F., Kjarsgaard, B. A., Romer, R. L., Heaman, L. M., Stracke, A. and Jenner, G. A. 2008. Between carbonatite and lamproite—Diamondiferous Torngat ultramafic lamprophyres formed by carbonate-fluxed melting of cratonic MARID-type metasomes. *Geochimica et Cosmochimica Acta*, **72**, 3258–3286.

Tappe, S., Romer, R. L., Stracke, A., Steenfelt, A., Smart, K. A., Muehlenbachs, K. and Torsvik, T. H. 2017. Sources and mobility of carbonate melts beneath cratons, with implications for deep carbon cycling, metasomatism and rift initiation. *Earth and Planetary Science Letters*, **466**, 152–167.

Tappe, S., Beard, C. D., Borst, A. M., Humphreys-Williams, E. R., Walter, B. F. and Yaxley, G. M. 2025. Kimberlite, carbonatite and alkaline magmatic systems: definitions, origins, and strategic mineral resources. EarthArXiv Preprints, https://eartharxiv.org/repository/ view/8658/

Taylor, H. P., Frechen, J. and Degens, E. T. 1967. Oxygen and carbon isotope studies of carbonatites from the Laacher See District, West Germany and the Alnö District, Sweden. *Geochimica et Cosmochimica Acta*, **31**, 407–430.

Upton, B. G. J., Craven, J. A. and Kirstein, L. A. 2006. Crystallisation of mela-aillikites of the Narsaq region, Gardar alkaline province, south Greenland and relationships to other aillikitic–carbonatitic associations in the province. *Lithos*, **92**, 300–319.

Vasyukova, O. V. and Williams-Jones, A. E. 2022. Carbonatite metasomatism, the key to unlocking the carbonatite-phoscorite-ultramafic rock paradox. *Chemical Geology*, **602**, https://doi.org/10.1016/j.chemgeo.2022.120888

Veksler, I. V., Nielsen, T. F. D. and Sokolov, S. V. 1998. Mineralogy of Crystallized Melt Inclusions from Gardiner and Kovdor Ultramafic Alkaline Complexes: Implications for Carbonatite Genesis. *Journal of Petrology*, **39**, 2015–2031.

Verwoerd, W. J. 1967. The carbonatites of South Africa and South West Africa. *Handbook of the Geological Survey of South Africa*, **6**, Government Printer, Pretoria, South Africa, 452 pp.

Verwoerd, W. J. 1993. Update on carbonatites of South Africa and Namibia. *South African Journal of Geology*, **96(3)**, 75–95.

Walter, B. F., Giebel, R. J., Steele-MacInnis, M., Marks, M. A., Kolb, J. and Markl, G. 2021. Fluids associated with carbonatitic magmatism: A critical review and implications for carbonatite magma ascent. *Earth-Science Reviews*, **215**, https://doi.org/10.1016/j.earscirev. 2021.103509

Walter, B., Giebel, R. J., Marlow, A., Siegfried, P., Marks, M., Markl, G., Palmer, M. and Kolb, J. 2022. The Keishöhe carbonatites of southwestern Namibia -the post-magmatic role of silicate xenoliths on REE mobilisation. *Communications of the Geological Survey of Namibia*, **25**, 1–31.

Walter, B. F., Giebel, R. J., Siegfried, P. R., Gudelius, D. and Kolb, J. 2023. The eruption interface between carbonatitic dykes and diatremes – The Gross Brukkaros volcanic field Namibia. *Chemical Geology*, **621**, https://doi.org/10.1016/j.chemgeo. 2023.121344

Walter, B. F., Giebel, R. J., Arthuzzi, J. C. L., Kemmler, L. and Kolb, J. 2024. Diatreme-hosted fluorite mineralization in S-Namibia

– A tale of cryogenic brine formation and fluid mixing below an unconformity in the context of Pangea rifting. *Journal of African Earth Sciences*, **210**, https://doi.org/10.1016/j.jafrearsci.2023.105154

Walter, B. F., Scharrer, M., Giebel, R. G., Beranoaguirre, A., Arthuzzi, J. C.L., Kemmler, L., Ladisic, A., Dück, S. Marks, M. and Markl, G. 2025. Sideritization and silification of unconformity-related hydrothermal baryte veins near Grünau, south Namibia. *Geochemistry*, **85**, https://doi.org/10.1016/j.chemer.2024.126244

Walter, M. J. 1998. Melting of Garnet Peridotite and the Origin of Komatiite and Depleted Lithosphere. *Journal of Petrology*, **39**, 29–60.

Webb, K. and Hetman, C. 2021. Magmaclasts in kimberlite. *Lithos*, **396–397**, https://doi.org/10.1016/j.lithos.2021.106197

Winter, F. and Rikhotso, C. T. 1998. *A review of kimberlite prospecting by De Beers companies in Namibia during the period 1971 to 1986*. Unpublished Report De Beers Consolidated Mines, 61 pp.

Woolley, A. R. and Kjarsgaard, B. A. 2008. Paragenetic types of carbonatite as indicated by the diversity and relative abundances of associated silicate rocks: evidence from a global database. *The Canadian Mineralogist*, **46**, 741–752.

Xie, Y., Ma, L., Zhao, G., Xie, C., Han, Y., Li, J., Liu, Q., Yao, J., Zhang, Y. and Lu, Y. 2020. Origin of the Heping granodiorite pluton: Implications for syn-convergent extension and asthenosphere upwelling accompanying the early Paleozoic orogeny in South China. *Gondwana Research*, **85**, 149–168.

Yaxley, G. M., Crawford, A. J. and Green, D. H. 1991. Evidence for carbonatite metasomatism in spinel peridotite xenoliths from western Victoria, Australia. *Earth and Planetary Science Letters*, **107**, 305–317.

Yaxley, G. M., Kjarsgaard, B. A. and Jaques, A. L. 2021. Evolution of Carbonatite Magmas in the Upper Mantle and Crust. *Elements*, **17**, 315–320.

Yaxley, G. M., Anenburg, M., Tappe, S., Decree, S. and Guzmics, T. 2022. Carbonatites: classification, sources, evolution, and emplacement. *Annual Review of Earth and Planetary Sciences*, **50(1)**, 261-293.

Yu, X., Chen, L.-H. and Zeng, G. 2015. Growing magma chambers control the distribution of small-scale flood basalts. *Scientific Reports*, **5**, https://doi.org/10.1038/srep16824

Zech, R. F., Onken, C. T., Sartori, G., Simon, S. J., Shipandeni, A., Galli, A., Spikings, R. A. and Schmidt, M. W. 2025. The age and source of Cambrian post-orogenic magmatism in the Kuboos-Bremen Igneous Province (Southern Namibia). *Journal of African Earth Sciences*, **226**, https://doi.org/10.1016/j.jafrearsci.2025.105592

Appendix 1. Sample locations of the Kuboos-Bremen Line intrusives from SE (No 1) to the NW (No. 9) listing main lithologies, age determinations and respective literature references

No.	**Locality**	**Main Lithology**	**Age** (Zech *et al*., 2025)	**Literature**
1	Swartbank Pluton	Granite	?	Söhnge and De Villiers, 1948
2	Kuboos Pluton	Granite, Syenite	507 Ma (Ar-Ar; Dunn, 2001)	Frimmel, 2000
3	Tatasberg Pluton	Granite	502 Ma (Ar-Ar; Dunn 2001)	Söhnge and De Villiers, 1948
4	Grootpenseiland Complex	Granite, Nepheline syenite, Syenite	501–507 Ma (U-Pb)	Smithies and Marsh, 1996
5	Marinkas Quelle Complex	Granite, Syenite	501–507 Ma (U-Pb)	Smithies and Marsh, 1996
		Carbonatite, Fenite	508–530 Ma (U-Pb)	Smithies and Marsh, 1996
6	Kanabeam Complex	Granite, Nepheline syenite, Syenite, Quartz syenite, Alkali monzonite, Alkali gabbro	500–509 Ma (U-Pb)	Reid, 1991
7	Mt. Ai Ais Breccia Pipe	Alkaline breccia pipes	?	Kröner and Blignault, 1976
8	Younger Bremen Complex	Granite, Nepheline syenite	493 and 496 Ma (U-Pb)	Middlemost, 1967
9	Kainab Alkaline Province	Carbonatite-Melilitite-Lamprophyre swarm	523 and 527 (Ar-Ar)	Schreuder, 1975

Appendix 2. List of all samples from the Garub valley, giving rock type, emplacement mode and coordinates, together with analytical methods used (TS - thin section, WR – whole rock analysis, µXRF – micro X-ray fluorescence, SEM – scanning electron microscopy, CL – cathodoluminescence, SI – stable isotope analysis)

Sample GRB…	**Rock type** (Macroscopic estimate)	**Emplacement mode**	**Locality**		**Analytical methods** applied
			Latitude	Longitute	
025	Ultramafic	Diatreme	27°27'31.15"S	18°55'58.95"E	TS, WR, µXRF, SEM
026A	Carbonatite breccia	Diatreme	27°27'35.31"S	18°55'58.00"E	TS, WR, SI, µXRF
026B	Limestone	Country rock	27°27'35.31"S	18°55'58.00"E	TS, WR, µXRF
026C	Siltstone	Country rock	27°27'35.31"S	18°55'58.00"E	TS, WR, µXRF
026D	Siltstone + carbonatite	Dyke	27°27'35.31"S	18°55'58.00"E	TS, µXRF
026E	Ultramafic	Dyke	27°27'35.31"S	18°55'58.00"E	TS, WR
026F	Siltstone + carbonatite	Contact	27°27'35.31"S	18°55'58.00"E	TS, WR, µXRF, SEM
027	Carbonatite with granite/gneiss	Diatreme	27°27'38.00"S	18°56'36.60"E	TS, WR, µXRF
028A	Ultramafic	Dyke	27°27'38.69"S	18°56'36.00"E	TS, WR, µXRF, SEM
028B	Ultramafic + carbonatite	Contact	27°27'38.69"S	18°56'36.00"E	TS, µXRF
028C	Carbonatite	Dyke	27°27'38.69"S	18°56'36.00"E	TS, WR, µXRF
029A	Limestone	Country rock	27°27'40.94"S	18°57'05.37"E	TS, WR
029B	ultramafic breccia	Diatreme	27°27'40.94"S	18°57'05.37"E	TS
030	Location only	Unconformity	27°27'40.79"S	18°57'05.02"E	
031	Carbonatite breccia	Pipe	27°27'37.81"S	18°57'18.81"E	TS, WR
032	Location only		27°27'40.72"S	18°57'31.14"E	
033A	Diatreme breccia	Diatreme	27°27'40.72"S	18°57'31.14"E	TS, µXRF, SEM
033B	Diatreme breccia	Diatreme	27°27'40.72"S	18°57'31.14"E	TS, WR, µXRF, CL, SEM
033C	Diatreme breccia	Diatreme	27°27'42.22"S	18°57'31.48"E	TS, WR, SI, µXRF
033D	Diatreme breccia + siltstone	Contact	27°27'42.22"S	18°57'31.48"E	TS, µXRF
034	Location only	Dyke	27°27'35.57"S	18°57'47.77"E	
035A	Diatreme breccia	Diatreme	27°27'35.57"S	18°57'47.77"E	TS, WR
035B	Ultramafic	Diatreme	27°27'35.57"S	18°57'47.77"E	TS, WR
035C	Diatreme breccia	Diatreme	27°27'35.57"S	18°57'47.77"E	TS, WR
036	Diatreme + granite/gneiss	Contact	27°27'35.04"S	18°57'47.13"E	TS, WR, µXRF, SEM
037A	Carbonatite	Dyke	27°27'33.52"S	18°58'30.13"E	TS, WR, EMPA
037B	Garnet bearing gneiss	Country rock	27°27'33.52"S	18°58'30.13"E	TS, WR, µXRF, CL, SEM
037C	Diatreme breccia	Diatreme	27°27'33.52"S	18°58'30.13"E	TS, WR, µXRF, CL, SEM
037D	Dolerite	Dyke	27°27'33.52"S	18°58'30.13"E	
038	Diatreme breccia	Diatreme	27°27'30.73"S	18°58'29.64"E	TS, WR, µXRF, CL, SEM
039A	Globular diatreme	Diatreme	27°27'30.43"S	18°58'44.20"E	TS, WR, µXRF, SEM, SI
039B1	diatreme	Diatreme	27°27'30.43"S	18°58'44.20"E	TS, WR, SI, µXRF
039B2	Carbonatite	Diatreme	27°27'30.43"S	18°58'44.20"E	TS, WR
040A	Diatreme breccia	Diatreme	27°27'24.09"S	18°59'28.46"E	TS, WR, µXRF
040B	Globular diatreme	Diatreme	27°27'24.09"S	18°59'28.46"E	TS, WR, SI, µXRF
040C	Garnet bearing gneiss	Country rock	27°27'24.09"S	18°59'28.46"E	
041A	Garnet bearing gneiss	Country rock/mine	27°27'37.85"S	18°59'47.92"E	WR
041B	Altered diatreme	Diatreme/mine	27°27'37.85"S	18°59'47.92"E	
042A	Dolerite	Dyke	27°27'27.57"S	19°00'11.63"E	TS, WR, µXRF
042B	Diatreme breccia	Diatreme	27°27'27.57"S	19°00'11.63"E	TS, WR, SI, µXRF
042C	Ultramafic	Diatreme	27°27'27.57"S	19°00'11.63"E	TS, WR, µXRF, SEM
042D1	Diatreme breccia	Diatreme	27°27'27.57"S	19°00'11.63"E	TS, WR
042D2	Diatreme breccia	Diatreme	27°27'27.57"S	19°00'11.63"E	TS, µXRF
043	Dolerite	Dyke	27°26'45.35"S	18°57'33.53"E	
043B	Ultramafic	Dyke	27°26'45.35"S	18°57'33.53"E	TS

044A	Carbonatite	Diatreme	27°26'43.53"S	18°57'33.31"E	TS, WR, SI
044B	Diatreme breccia	Diatreme	27°26'43.53"S	18°57'33.31"E	TS, WR, µXRF, SEM
045	Dolerite	Dyke	27°26'39.73"S	18°56'55.91"E	

Appendix 3. Part one of the results from whole-rock analysis conducted on the 35 selected Garub samples

Sample	**25**	**026A**	**026E**	**026F2**	**27**	**028A**	**028C**	**31**	**033B**	**033C**	**035A**	**035B**
(GRB...)	Diatreme	Diatreme	Diatreme	Diatreme	Diatreme	Diatreme	Diatreme	Diatreme	Diatreme	Diatreme	Diatreme	Diatreme
Major elements (wt.%)												
Na_2O	2.95	3.79	2.05	2.60	3.93	1.88	0.06	< 198 PPM	3.92	0.98	3.12	2.96
MgO	9.02	6.22	8.20	9.07	7.80	5.89	6.18	8.04	5.95	6.36	8.06	7.89
Al_2O_3	7.82	7.29	6.50	5.65	6.86	6.46	5.85	5.73	8.15	7.52	6.23	7.44
SiO_2	35.19	31.94	27.76	19.77	28.00	28.85	30.16	24.35	34.20	24.00	26.09	30.91
P_2O_5	1.23	1.27	1.78	0.96	1.27	1.27	1.16	1.16	0.90	1.38	1.08	1.21
K_2O	1.43	0.05	2.97	0.08	0.58	0.08	1.37	0.52	0.93	2.05	0.14	0.92
CaO	13.70	13.86	16.87	18.64	15.13	19.71	17.49	18.06	13.14	16.24	15.79	12.91
TiO_2	3.43	3.64	3.86	3.29	3.60	3.63	3.47	3.30	3.02	3.96	3.24	3.71
Mn_2O_3	0.25	0.23	0.36	0.22	0.23	0.24	0.22	0.22	0.21	0.24	0.24	0.22
Fe_2O_3	12.79	12.81	14.85	12.23	12.91	13.14	11.29	12.63	10.85	13.54	11.43	13.04
LOI	11.08	18.10	13.44	26.10	18.45	17.06	21.89	24.01	18.58	22.55	23.76	17.64
C	2.55	4.97	3.13	7.21	4.98	4.96	5.32	6.23	4.97	5.64	6.64	4.72
S	0.07	0.04	0.10	0.06	0.03	0.21	0.06	0.03	0.03	0.03	0.04	0.03
Total	**99.78**	**99.76**	**99.62**	**99.27**	**99.39**	**99.14**	**99.62**	**98.34**	**100.27**	**99.31**	**99.70**	**99.37**
Trace elements (ppm)												
Li	236	51.8	306	67.3	83.5	277	34.0	107	31.9	56.7	19.3	71.9
Be	8.1	6.5	9.7	1.6	6.3	4.9	2.3	1.2	3.7	8.8	3.5	7.9
Sc	39.8	47.6	66.9	45.6	47.3	49.8	44.8	46.5	43.1	52.5	44.3	50.4
Ti	39543	49351	45693	46815	48020	51224	46909	45540	36570	54415	43869	48821
V	587	580	752	873	596	667	538	561	348	652	488	622
Cr	634	439	329	521	416	574	465	451	456	526	446	528
Mn	3737	3457	5313	3405	3324	3617	3285	3356	3144	3600	3604	3232
Co	96.8	91.0	98.2	91.7	106	97.6	72.3	81.5	72.9	101	83.1	94.6
Ni	237	148	131	144	148	157	122	139	122	167	125	161
Cu	231	235	216	381	234	261	111	8.5	79	226	191	243
Zn	235	249	249	299	212	216	226	278	196	266	161	224
Rb	173.2	3.5	234.5	10.7	48.5	10.3	109.8	43.1	42.0	159	11.5	61.1
Sr	3428	2322	3570	3598	2822	4394	859	553	1634	2758	2504	1991
Y	64.6	64.9	78.1	51.4	60.1	59.9	55.1	55.8	58.5	66.8	60.4	63.1
Zr	745	726	865	417	739	805	715	695	597	867	666	792
Nb	87	290	139	281	257	311	277	261	117	306	249	293
Mo	0.3	0.6	3.0	64.3	0.4	1.0	4.3	3.4	0.8	5.5	1.4	4.6
Ag	0.3	0.2	0.1	0.5	0.2	0.3	0.2	0.1	0.1	0.2	0.1	0.2
Ag	0.2	0.4	0.1	0.7	0.4	0.5	0.3	0.3	0.2	0.4	0.3	0.3
Cd	0.8	0.7	0.7	1.0	0.8	0.9	0.8	1.2	1.2	1.1	0.7	0.8
Sb	2.0	<0.067	<0.067	2.3	<0.067	<0.067	<0.067	<0.067	<0.067	<0.067	<0.067	<0.067
Cs	56.2	0.3	11.9	1.7	3.0	1.7	3.5	0.5	0.4	2.6	0.2	1.6
Ba	2842	1209	3914	363	1310	800	1161	270	806	566	94	1672
Hf	12.5	16.5	14.3	11.8	16.7	18.4	16.6	15.5	13.5	19.9	15.4	18.5
Ta	7.0	18.8	8.4	18.4	17.4	20.3	18.6	17.2	8.7	21.1	16.4	19.4
W	0.6	1.8	0.9	8.3	3.4	1.9	5.1	3.5	2.0	31.8	3.3	1.9
Pb	30.7	13.7	9.5	62.1	13.9	15.1	23.1	21.9	26.6	65.3	9.8	14.5
Bi	0.1	0.1	0.1	0.2	0.1	0.1	0.1	0.1	0.2	0.2	0.1	0.1
Th	34.5	34.3	22.9	27.1	30.8	31.2	28.7	27.8	25.4	35.4	28.7	31.8
U	4.1	10.0	9.3	6.5	5.9	4.7	10.1	8.8	9.2	9.6	6.7	6.5
REE												
La	261	244	222	214	241	253	230	235	198	277	223	243
Ce	496	484	424	408	471	487	443	457	385	537	431	472

Pr	58.7	58.8	50.5	48.3	55.9	57.9	52.9	54.7	46.3	64.2	51.2	56.6
Nd	218	222	189	182	212	217	198	206	175	244	194	212
Sm	37.4	38.6	32.5	30.2	36.6	36.6	33.8	35.0	30.5	41.7	33.6	36.3
Eu	10.0	10.2	9.1	8.0	9.9	10.0	9.5	9.8	7.9	11.5	9.1	9.6
Gd	26.8	27.5	24.1	21.1	26.3	26.2	24.2	25.4	22.3	30.2	24.5	26.1
Tb	3.3	3.4	3.1	2.6	3.3	3.2	3.0	3.1	2.9	3.7	3.1	3.2
Dy	15.8	16.3	16.0	12.8	15.7	15.5	14.4	14.8	14.3	17.6	15.2	16.0
Ho	2.6	2.7	2.9	2.1	2.6	2.6	2.4	2.4	2.4	2.9	2.6	2.7
Er	6.3	6.4	7.6	5.0	6.0	6.0	5.5	5.4	6.1	6.5	6.1	6.4
Tm	0.8	0.8	1.0	0.6	0.7	0.7	0.6	0.6	0.8	0.8	0.8	0.8
Yb	4.5	4.3	5.9	3.4	4.0	4.0	3.6	3.5	4.6	4.3	4.2	4.6
Lu	0.6	0.6	0.8	0.5	0.6	0.6	0.5	0.5	0.6	0.6	0.6	0.7
REE (tot)	**1141**	**1120**	**989**	**938**	**1086**	**1120**	**1023**	**1053**	**896**	**1242**	**999**	**1090**

Appendix 4. Part two of the results from whole-rock analysis conducted on the 35 selected Garub samples

Sample	**035C**	**036A**	**37A**	**037C**	**38**	**039A**	**039B1**	**039B2**	**040A**	**040B**	**042B**	**042C**
(GRB...)	Diatreme	Diatreme	Diatreme	Diatreme	Diatreme	Diatreme	Diatreme	Diatreme	Diatreme	Diatreme	Diatreme	Diatreme
Major elements (wt.%)												
Na_2O	3.48	1.64	< 208 PPM	2.61	2.79	6.07	< 208 PPM	1.33	0.02	0.28	2.79	1.71
MgO	6.61	5.55	8.68	7.26	7.22	2.07	7.35	6.70	6.84	7.25	7.16	6.99
Al_2O_3	6.67	6.11	5.91	7.61	7.62	10.94	6.52	6.28	5.71	5.86	6.80	6.97
SiO_2	29.98	32.06	27.29	34.43	34.69	38.93	29.19	27.39	21.92	25.65	21.19	25.46
P_2O_5	1.17	1.29	1.28	0.92	0.86	0.48	1.58	1.47	1.11	1.22	1.39	1.37
K_2O	0.13	1.48	1.32	2.10	1.87	0.10	1.17	0.84	3.73	3.96	0.08	0.84
CaO	14.46	16.69	14.75	14.22	14.11	14.24	15.00	18.32	20.45	16.87	19.53	18.72
TiO_2	3.55	3.47	4.26	2.90	2.77	2.84	3.98	3.51	3.01	3.11	3.07	3.25
Mn_2O_3	0.21	0.16	0.27	0.19	0.18	0.29	0.26	0.38	0.23	0.23	0.31	0.21
Fe_2O_3	12.39	9.90	14.55	6.95	7.01	8.56	13.49	9.62	10.02	11.63	11.32	14.69
LOI	20.50	20.34	20.93	20.27	20.17	15.01	20.44	23.22	25.24	22.41	24.14	17.64
C	5.34	5.41	5.46	5.33	5.34	3.60	5.00	5.82	6.55	5.91	6.08	4.28
S	0.20	0.02	0.02	0.01	0.01	0.06	0.08	0.09	0.01	0.08	0.15	0.08
Total	**100.07**	**99.03**	**99.57**	**99.84**	**99.66**	**100.08**	**99.45**	**99.65**	**98.62**	**99.12**	**98.44**	**98.64**
Trace elements (ppm)												
Li	23.4	35.3	131	11.5	11.6	8.8	94.6	34.0	24.1	12.7	28.7	123.9
Be	5.1	2.5	8.0	3.8	3.8	1.7	5.8	4.5	3.0	2.0	2.6	4.6
Sc	47.8	49.7	44.2	41.3	44.9	44.0	46.3	47.9	40.8	43.0	46.3	48.1
Ti	47500	46499	57439	36663	34717	36923	54720	50239	39779	39906	39496	34264
V	642	417	624	448	456	182	637	634	328	425	319	606
Cr	492	381	470	327	296	177	408	290	266	271	330	245
Mn	3140	2467	4029	2799	2668	4263	3961	5879	3465	3366	4869	3206
Co	82.4	66.9	90.5	50.3	47.9	99.4	86.0	56.2	62.3	60.7	80.4	99.9
Ni	145	133	179	93	88	111	155	79	69	62	110	118
Cu	232	195	217	28	20	253	246	45	510	157	67	228
Zn	218	237	318	230	222	115	242	105	153	117	420	268
Rb	12.6	72.1	132.1	57.8	51.6	7.8	140	105	202	203	5.8	61.9
Sr	2408	1623	667	1433	1386	425	822	1412	1512	2471	1911	3458
Y	57.1	85.0	61.4	59.9	65.7	54.5	67.8	78.4	61.7	59.6	61.0	66.7
Zr	719	792	649	674	854	437	826	961	643	784	552	622
Nb	309	237	345	179	172	235	333	290	268	259	60	26
Mo	2.7	12.7	5.6	2.4	2.5	15.7	1.0	0.5	2.9	0.8	2.2	0.3
Ag	0.2	0.3	0.2	0.2	0.2	0.3	0.2	0.2	0.1	0.1	0.1	0.2
Ag	0.4	0.4	0.4	0.3	0.3	0.5	0.4	0.3	0.3	0.3	0.1	0.1
Cd	1.1	1.0	1.2	1.0	1.3	0.7	0.9	1.0	0.7	0.9	1.1	0.6
Sb	<0.067	<0.067	<0.067	<0.067	<0.067	<0.067	<0.067	<0.067	<0.067	<0.067	<0.067	<0.067
Cs	0.4	0.3	1.8	0.9	0.9	0.3	2.1	1.1	0.3	0.3	0.3	1.3
Ba	368	330	458	326	309	3610	413	1495	935	1972	171	2507
Hf	17.2	16.8	14.8	18.2	24.3	9.8	17.9	19.1	17.2	17.9	10.5	10.4
Ta	20.0	15.9	24.6	11.7	11.0	16.0	22.6	19.0	16.0	16.0	3.7	2.2

W	3.7	4.6	13.2	8.6	9.4	3.1	1.8	3.0	37.4	26.9	15.0	1.0
Pb	16.4	52.3	47.4	34.7	29.0	42.3	18.5	18.3	16.8	13.9	30.6	28.5
Bi	0.2	0.4	0.1	0.0	0.0	0.4	0.0	0.1	<0.002	<0.002	0.0	0.1
Th	30.0	41.9	39.2	28.9	29.5	34.4	38.1	36.6	28.6	28.8	33.0	34.1
U	7.7	24.3	9.3	8.1	9.7	12.5	10.9	6.7	4.3	3.9	3.6	8.9
REE												
La	233	223	296	200	188	232	306	309	227	235	267	276
Ce	454	436	594	386	361	443	596	610	437	452	502	528
Pr	53.8	52.5	70.7	46.0	42.9	50.1	70.3	71.7	52.7	53.9	59.3	63.2
Nd	203	200	266	172	162	175	263	261	201	205	220	240
Sm	34.9	36.6	44.4	29.4	28.4	25.6	45.3	40.3	34.7	35.1	36.8	40.9
Eu	9.6	11.6	12.1	7.9	7.5	4.5	12.7	10.9	9.6	9.7	10.0	11.1
Gd	24.9	28.1	30.2	21.8	21.5	17.7	31.7	29.6	24.9	25.5	26.9	29.2
Tb	3.1	3.8	3.6	2.8	2.9	2.3	3.8	3.8	3.1	3.2	3.3	3.6
Dy	14.8	19.9	16.9	14.3	14.9	11.9	17.7	19.0	15.4	15.2	15.9	17.1
Ho	2.5	3.5	2.7	2.5	2.7	2.1	2.9	3.2	2.6	2.6	2.6	2.8
Er	5.8	8.7	6.1	6.2	7.1	5.9	6.8	7.6	6.1	6.0	6.2	6.7
Tm	0.7	1.1	0.7	0.8	0.9	0.9	0.8	0.9	0.7	0.7	0.8	0.8
Yb	3.9	6.3	3.7	4.6	5.6	5.8	4.4	5.1	4.1	4.0	4.1	4.5
Lu	0.6	0.9	0.5	0.7	0.8	0.9	0.6	0.7	0.6	0.6	0.6	0.6
REE (tot)	**1044**	**1032**	**1347**	**896**	**846**	**979**	**1362**	**1374**	**1019**	**1048**	**1156**	**1224**

Appendix 5. Part three of the results from whole-rock analysis conducted on the 35 selected Garub samples

Sample	**042D1**	**044A**	**044B**	**026B**	**026C**	**026F1**	**029A**	**036B**	**037B**	**041A**	**042A**
(GRB...)	Diatreme	Diatreme	Diatreme	Limestone	Siltstone	Siltstone	Limestone	"Fenite"	Gneiss	Gneiss	Dolerite
Major elements (wt.%)											
Na_2O	2.58	0.05	0.70	0.00	4.41	8.62	0.32	7.32	1.37	1.77	1.07
MgO	6.37	8.97	9.82	16.20	2.08	3.38	14.34	3.99	1.87	1.83	9.16
Al_2O_3	6.42	6.13	7.16	0.62	8.83	14.43	1.65	13.13	16.33	16.93	16.29
SiO_2	20.63	27.31	19.88	5.72	71.20	53.58	6.81	49.57	70.03	67.19	48.47
P_2O_5	1.35	1.24	1.31	0.02	0.39	0.02	0.04	0.04	0.09	0.11	0.07
K_2O	0.06	1.49	1.11	0.12	0.26	0.05	0.25	0.44	3.87	3.99	0.68
CaO	20.27	15.25	17.25	25.35	6.02	5.42	26.65	8.26	1.00	1.01	11.33
TiO_2	3.10	3.44	3.61	0.02	0.88	0.66	0.05	0.52	1.09	0.95	0.45
Mn_2O_3	0.29	0.32	0.79	0.85	0.06	0.18	1.12	0.12	0.10	0.09	0.18
Fe_2O_3	14.21	12.79	12.12	3.24	2.68	4.34	4.33	3.45	7.26	7.14	10.00
LOI	23.37	21.71	24.69	41.79	7.51	8.98	40.08	12.53	1.74	1.64	0.37
C	6.16	5.81	6.21	11.85	1.98	2.43	11.56	3.49	0.04	0.13	0.07
S	0.03	0.11	0.14	0.02	0.05	0.08	0.05	0.01	0.01	0.11	0.07
Total	**99.16**	**99.43**	**99.75**	**94.07**	**104.79**	**99.92**	**95.96**	**99.53**	**105.06**	**102.98**	**98.43**
Trace elements (ppm)											
Li	39.0	86.1	66.3	6.4	25.5	102.1	9.3	18.0	110	102	22.4
Be	2.2	3.4	2.1	1.2	2.1	3.6	1.5	2.2	14.4	12.5	1.3
Sc	45.6	44.9	48.5	1.5	20.0	23.8	3.7	12.5	34.6	28.1	87.9
Ti	38171	48643	48638	425	8071	8499	914	6810	13237	11991	5993
V	510	589	558	18	83	241	34	132	168	218	445
Cr	218	577	546	8	92	118	10	107	158	147	1102
Mn	4500	4894	11877	13648	770	2620	17386	1742	1249	1267	2747
Co	112	93.0	75.4	6.6	14.5	29.9	13.0	18.3	36.1	39.9	107
Ni	110	219	175	14	27	64	21	26	88	93	404
Cu	217	224	734	4	62	58	18	42	117	117	312
Zn	225	252	464	124	110	183	95	92	183	228	141
Rb	3.2	141	99.7	11.3	19.2	1.2	22.6	24.8	278	345	154
Sr	2474	2985	1384	439	649	826	541	810	197	206	195
Y	67.1	58.0	68.4	14.2	57.3	21.0	25.5	12.8	71.5	58.1	25.2
Zr	640	686	854	13	461	201	26	298	495	461	74
Nb	120	312	308	<0.213	3	23	3	25	41	37	10
Mo	2.4	6.1	4.7	1.4	7.8	41.9	3.2	3.2	2.0	2.9	0.3
Ag	0.1	0.2	0.2	0.3	0.2	0.2	0.0	0.1	0.2	0.2	0.2

Ag	0.2	0.4	0.4	0.3	0.1	0.2	0.1	0.1	0.1	0.2	0.2
Cd	0.7	1.2	2.4	1.4	0.5	0.5	1.8	0.5	0.4	0.4	0.2
Sb	<0.067	<0.067	<0.067	<0.067	<0.067	2.0	<0.067	<0.067	<0.067	<0.067	<0.067
Cs	0.1	1.7	3.8	0.5	0.7	0.3	1.6	1.4	4.2	5.8	3.8
Ba	138	1413	9123	142	2265	91	2160	162	1402	1263	663
Hf	12.1	15.3	17.3	0.4	11.3	5.9	0.7	9.0	14.8	13.6	2.5
Ta	8.7	21.4	20.5	<0.024	<0.024	1.3	<0.024	1.3	2.0	2.8	0.7
W	8.1	3.6	2.8	0.4	1.3	6.1	0.7	1.3	0.5	1.0	0.7
Pb	22.8	55.0	54.0	37.2	44.6	31.6	24.7	52.2	49.1	73.0	8.4
Bi	0.1	0.1	1.1	0.1	0.4	0.2	0.2	0.2	0.1	0.2	0.2
Th	28.8	35.4	36.6	1.4	31.9	13.3	3.0	60.2	49.7	43.6	3.0
U	5.4	9.0	22.6	3.1	6.8	3.5	3.1	5.4	5.2	4.8	1.3
REE											
La	252	276	266	6.1	56.2	57.9	13.1	125	118	98.4	11.2
Ce	479	524	499	13.0	127	112	28.2	271	246	212	26.9
Pr	57.4	61.9	59.3	1.5	15.4	13.8	3.4	34.5	29.9	26.2	3.5
Nd	216	231	220	6.3	61.1	51.8	14.0	131	114	99	14.9
Sm	36.9	38.4	39.5	1.7	13.1	8.9	3.8	24.2	22.6	19.6	4.6
Eu	10.0	10.6	11.3	0.4	2.3	1.5	0.8	2.2	2.9	3.1	1.1
Gd	26.7	26.8	30.2	2.2	12.6	5.7	4.5	13.0	17.9	14.5	4.7
Tb	3.4	3.3	3.8	0.4	1.9	0.8	0.8	1.1	2.6	2.1	0.8
Dy	17.0	15.5	17.7	2.4	11.1	4.2	4.7	3.8	14.4	12.1	4.9
Ho	2.9	2.5	2.9	0.5	2.2	0.8	0.9	0.5	2.9	2.3	1.0
Er	6.9	5.7	6.5	1.3	6.5	2.4	2.5	1.2	8.2	6.7	3.1
Tm	0.8	0.7	0.8	0.2	1.0	0.4	0.4	0.1	1.2	1.0	0.5
Yb	4.6	3.7	4.2	1.1	6.2	2.7	2.2	0.9	7.9	6.3	3.0
Lu	0.6	0.5	0.6	0.2	1.0	0.5	0.3	0.1	1.3	1.0	0.5
REE (tot)	**1114**	**1202**	**1162**	**37.2**	**318**	**264**	**79.6**	**609**	**589**	**505**	**80.7**

Appendix 6. List of samples analysed for stable isotopes, including number of cycles (n) and corresponding $\delta^{13}C_{PDB}$ [‰] and $\delta^{18}O_{SMOW}$ [‰] values, along with their standard deviations (SD)

Sample (GRB...)	**n**	**$\delta^{13}C_{PDB}$ [‰]**	**SD**	**$\delta^{18}O_{SMOW}$ [‰]**	**SD**
026A	10	-3.63	0.06	15.60	0.07
033C	10	-3.17	0.08	17.05	0.13
039A	10	-3.58	0.07	26.34	0.06
039B	10	-0.84	0.06	19.49	0.06
040B	10	-2.20	0.03	19.04	0.06
042B	10	-1.74	0.09	20.43	0.08
044A	10	-4.08	0.05	15.14	0.07